CANCER

Spatially resolved analysis of microenvironmental gradient impact on cancer cell phenotypes

Jamie Auxillos[1,2]†, Roxane Crouigneau[3]†, Yan-Fang Li[4]†, Yifan Dai[1,2], Arnaud Stigliani[1,2], Isabella Tavernaro[5], Ute Resch-Genger[5], Albin Sandelin[1,2]*, Rodolphe Marie[4]*, Stine F. Pedersen[3]*

Despite the physiological and pathophysiological significance of microenvironmental gradients, e.g., for diseases such as cancer, tools for generating such gradients and analyzing their impact are lacking. Here, we present an integrated microfluidic-based workflow that mimics extracellular pH gradients characteristic of solid tumors while enabling high-resolution live imaging of, e.g., cell motility and chemotaxis, and preserving the capacity to capture the spatial transcriptome. Our microfluidic device generates a pH gradient that can be rapidly controlled to mimic spatiotemporal microenvironmental changes over cancer cells embedded in a 3D matrix. The device can be reopened allowing immunofluorescence analysis of selected phenotypes, as well as the transfer of cells and matrix to a Visium slide for spatially resolved analysis of transcriptional changes across the pH gradient. This workflow is easily adaptable to other gradients and multiple cell types and can therefore prove invaluable for integrated analysis of roles of microenvironmental gradients in biology.

INTRODUCTION

Microenvironmental gradients, such as local gradients of oxygen, pH, lactate, or signaling molecules, play key roles in normal physiological processes, such as fetal development and immune function (*1*, *2*), and in diseases, with cancer as a prime example. The in-depth understanding of tumor metabolic, cellular, and genetic heterogeneity has surged in recent years, driven by advances in single-cell sequencing and metabolic sensors (*3*, *4*). Spatiotemporally heterogeneous gradients of oxygen, pH, lactate, other metabolites, and signaling molecules exist in most if not all solid tumors, largely determine the immediate tumor microenvironment (TME), and largely control disease progression (*5*, *6*). Work by us and others point to the essential contributions of acidic extracellular pH (pH_e) (*6*–*9*), hypoxia (*10*), and lactate (*11*, *12*) in determining cancer aggressiveness, metastasis, and chemotherapy resistance (*7*, *13*–*15*). Differently from each gradient alone, combinations of such gradients determine cancer aggressiveness (*16*) including cancer stem cell properties (*17*).

In vivo profiling of such gradients is very challenging. Moreover, the causal impact of gradients on cell phenotypes, or vice versa, cannot be established since neither cell diversity nor gradients can be controlled in vivo. Therefore, in vitro methods for subjecting cells to precise, multidimensional, and multicomponent gradients are needed. However, spatial gradients are difficult to establish in macroscopic experimental setups, and temporal gradient modulation is even more challenging. Gradients are best established via diffusion, which is slow for large distances and easily disturbed by convection. This has driven the application of microfluidics to create chemical gradients on the submillimeter scale. Microfluidic devices offer laminar flow conditions that allow the decoupling of diffusion and convection across flow direction at high Peclet number. In addition, microfluidic device formats are suitable for live-cell imaging, enabling detailed studies of cell behaviors in gradients, such as chemotaxis. Solute gradients in microfluidic devices have been created by combining dilution series in a single channel with cells (*18*, *19*), yet this imposes shear stress on cells that can induce artifacts. Alternatively, cells can be isolated in nanoliter well arrays (*20*), embedded in a hydrogel (*21*), or gradients can be established by diffusion only (*22*, *23*). However, the current systems are not well suited for studying the impact of microenvironmental gradients on cell phenotypes. pH gradient systems are still lacking, and with few exceptions (*21*), phenotype analysis is limited to optical imaging. Thereby, crucial information, such as gradient-dependent changes in gene expression patterns, is lost. Moreover, the vast majority of microfluidic platforms are sealed, precluding retrieval of, or access to, cells for further analysis. This aspect in particular prevents the combination with cell-based assays to study, e.g., biological processes such as apoptosis, the location of specific marker proteins, and changes in gene expression as function of the spatial position of the cells within gradients. Thus, for an in-depth understanding of the causal roles of gradients in cancer progression and TME heterogeneity, flexible microfluidic systems are needed that can generate robust gradients and permit the application of spatially resolved functional and genomics assays across relevant microenvironmental gradients.

To this end, we present a workflow for in vitro modeling of TME gradients, using pH as an example of a small-molecule gradient highly relevant for TME. We designed a microfluidic device that enables the creation of a pH gradient over cells embedded in a collagen I layer in an $^1/_4$-cm^2 area and can be reversibly sealed. The device allows for optical imaging to characterize the gradient and studying chemotaxis and other cell phenotypes. The reversible sealing of the microfluidic platform allows subsequent analysis of the RNA and protein expression levels in these cells, retaining spatial information throughout the experiment. While we demonstrate here the integrated use of the system and representative protocols for subsequent assays, the modular design of this workflow from individual device components and its versatile combination of different assays enable diverse experimental designs and future extensions.

[1]Section for Computational and RNA biology, Department of Biology, University of Copenhagen, Denmark. [2]Biotech Research and Innovation Centre (BRIC), University of Copenhagen, Denmark. [3]Section for Cell Biology and Physiology, Department of Biology, University of Copenhagen, Denmark. [4]Department of Health Technology, Technical University of Denmark, 2800 Kgs. Lyngby, Denmark. [5]Division Biophotonics, Bundesanstalt für Materialforschung und -prüfung, Richard-Willstaetter Str. 11, 12489, Berlin, Germany.
*Corresponding author. Email: sfpedersen@bio.ku.dk (S.F.P.); rcwm@dtu.dk (R.M.); albin@bio.ku.dk (A.S.)
†These authors contributed equally to this work.

RESULTS

Overview of the workflow

Figure 1 provides an overview of our integrated workflow for pH gradient generation and analysis: A microfluidic device generates the desired pH gradient (in our case, pH 7.4 to 6.0). A collagen I/cell layer with dimensions exactly matching the gradient area is prepared on a glass slide compatible with optical imaging (Fig. 1A). The two components are assembled by a metal frame and a poly(methyl methacrylate) (PMMA) chip holder coupled to the perfusion system, resulting in the rapid generation of the gradient and allowing optical imaging analysis of, e.g., cell migration (Fig. 1B). The device can be disassembled without damage to the cells, for further phenotypic analyses requiring cell access, such as immunofluorescence (IF) imaging (Fig. 1C). For spatial transcriptomic analysis [reviewed in (*24*); Fig. 1D], the collagen I/cell layer can be transferred to the capture area of a Visium gene expression (GEX) slide, the most commonly used commercially available spatial transcriptomic platform, or equivalent systems. The various components of the workflow are described and characterized in detail below.

Microfluidic device design

The particular design challenges that we addressed were to create a device that, firstly, exposes cells to a robustly generated chemical gradient through microfluidics, and second, allows for retrieval of the cells for subsequent experiments after their exposure to the gradient. For goal II, device sealing had to be reversible, and the size of the cell exposure area should be compatible with the requirements imposed by subsequent assays such as the Visium GEX slide for spatial transcriptomics.

To this end, we designed a two-part platform consisting of (i) an elastomeric microfluidic gradient device that produced a pH gradient across a 5 mm by 5 mm transparent observation area and (ii) a glass "lid" that contained cells. Here, we used MDA-MB-231 breast cancer cells embedded in a 150-μm-thick collagen I gel layer (Fig. 2, A to C). The gradient device and lid were reversibly assembled using a top and bottom layer and screws, and the gradient observation area and the collagen I layer were subsequently aligned by naked eye (Fig. 2, A and D). The microfluidic gradient device was equipped with two inlets for solutions of pH 6.0 and 7.4 (Fig. 2B), which were then divided and

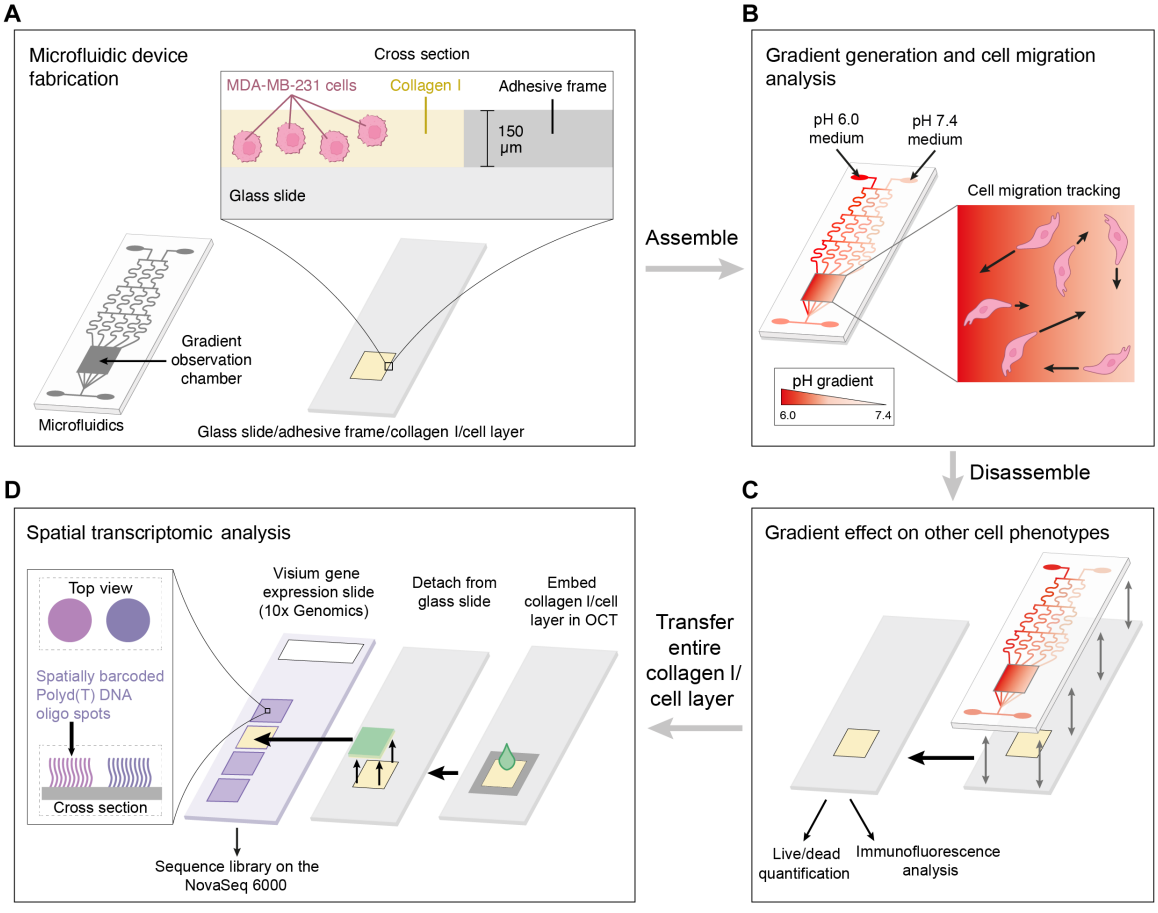

Fig. 1. Overview of the integrated microfluidic workflow. (**A**) The microfluidic device was cast in polydimethylsiloxane (PDMS) on a clean room microfabricated mold. The cells were cultured in a 150-μm-thick collagen I layer deposited on a glass slide to match the gradient area. (**B**) The PDMS microfluidic device and the glass slide containing the collagen I/cell layer were assembled in a metal frame holder and perfused with growth media of pH 7.4 and 6.0 through the inlet channels, in a CO_2 incubator or in the environmentally controlled chamber of an epifluorescence microscope. This allowed rapid formation of a constant pH gradient across the observation chamber, through which cells could be monitored by live imaging and migration parameters analyzed. (**C**) Disassembly of the device could be performed without damage to the cells in the collagen I layer, which were subsequently analyzed using either live/dead staining or IF analysis. (**D**) Alternatively, the collagen I/cell layer was frozen in optimal cutting temperature (OCT) compound and transferred as an OCT/collagen I block to a GEX slide for spatial transcriptomic analysis.

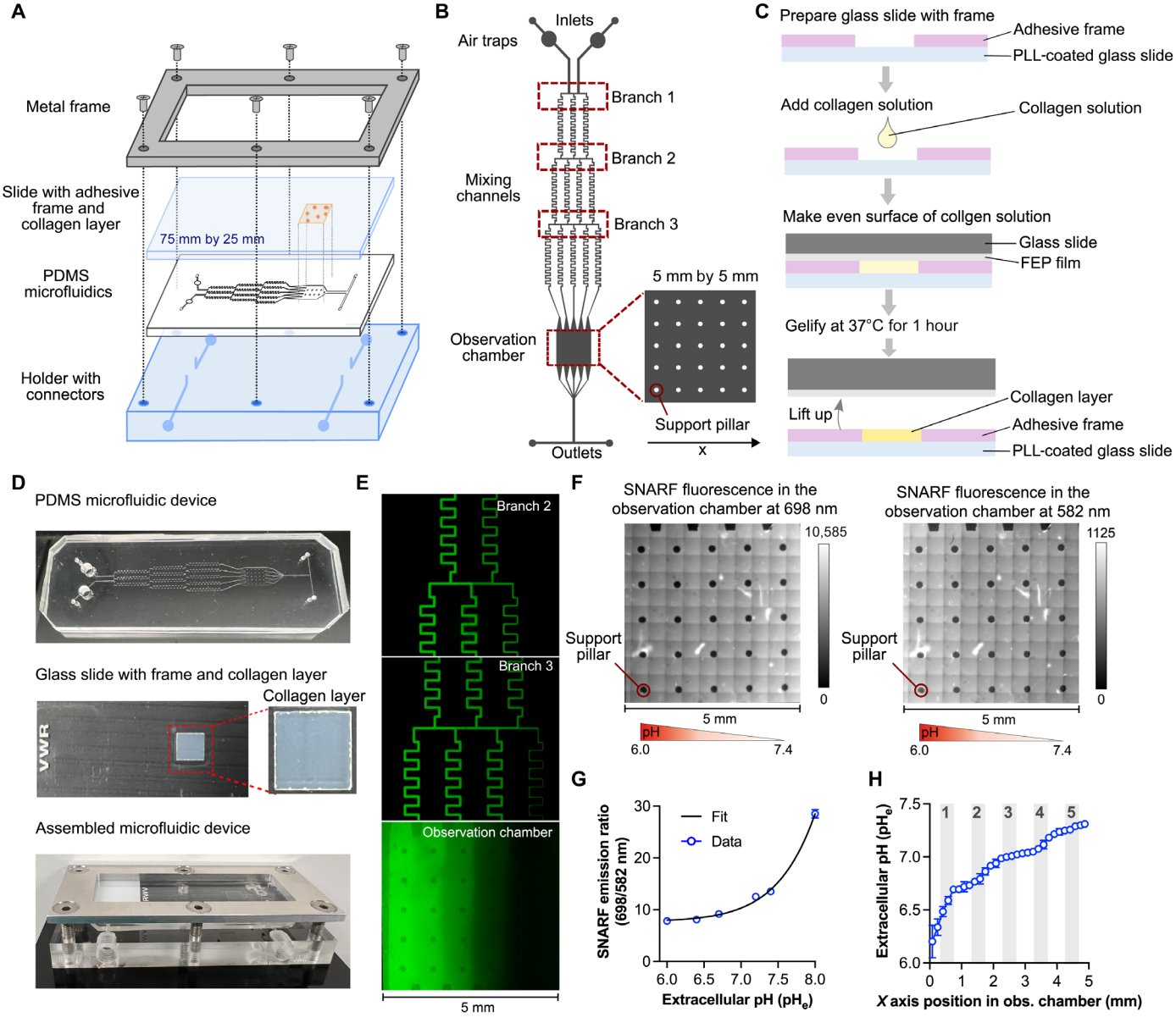

Fig. 2. Development of a reversible-sealing microfluidic device for spatiotemporal gradient generation. (**A**) Schematic exploded view of the microfluidic device consisting of a (i) metal frame, (ii) glass slide with an adhesive frame defining a collagen I slab with cells, (iii) PDMS microfluidic layer with channels to form the pH gradient, and (iv) PMMA chip holder with fluidic connections. Screws hold the assembly together. (**B**) Schematic overview of the microfluidic channel design comprising two inlets, air traps for potential air bubbles, mixing channels for dividing and mixing solutions into a dilution series, an observation chamber where the gradient is generated along the x direction, and outlets. The 5 × 5 mm observation chamber matches the GEX slide's size for spatial transcriptomic analysis. Support pillars with a 200-μm-diameter prevent the observation chamber of collapsing. (**C**) Process flow for collagen I layer preparation (here shown without cells). (**D**) Photos of (from top) the PDMS microfluidic device, the glass slide with the collagen I layer, and the assembled microfluidic device. (**E**) Fluorescence image of fluorescein at branch 2, branch 3, and the observation chamber. (**F**) Fluorescence images of SNARF in the gradient observation chamber at two different emission wavelengths. Black dots show the positions of support pillars. (**G**) Calibration of the SNARF ratiometric (698/582 nm) signal as function of pH (mean with SEM error bars) and a fitting line. (**H**) Measured pH gradient across the observation channel (mean with SD error bars). Gray areas show the positions 1 to 5 used for cell phenotype imaging.

mixed in a set of bifurcating mixing channels, thereby creating a pH gradient across the gradient observation channel. The microfluidic device was fabricated by polydimethylsiloxane (PDMS) casting on a clean room microfabricated SU-8 mold (*25*), providing micrometer control over device dimensions (fig. S1). A similar mold can be obtained via three-dimensional (3D) printing, making it accessible for labs with no access to a clean room facility (fig. S7). The PDMS device had a thickness of 4 mm to improve its stiffness. We assembled the device using a precise torque not exceeding 4 N·m on 4-mm screws (Fig. 2, A and D), limiting the deformation of the PDMS microfluidic channel and mechanical constraints on the collagen I/cell layer while maintaining a tight sealing. The collagen I/cell layer was made to have

a homogeneous thickness. Thereby, the observation chamber height remained constant when assembled on the chip holder with fluidic connections (Fig. 2, A and D). As detailed below, the cells were seeded by mixing with collagen I. Once the collagen I had gelated, the collagen I/cell culture layer was covered by a cell growth medium and kept in a CO_2 incubator until use.

To verify the ability of the device to generate stable gradients across the observation area and ensure a constant height of the chamber over the collagen I layer, we first used fluorescein sodium salt to characterize the device. A stable, step-like gradient of fluorescein was observed (Fig. 2E), which was stable for at least 24 hours, i.e., the longest time used in these tests. We next used the device to create a pH 7.4 to 6.0 gradient, which was visualized by adding the 40 mM small molecule pH indicator 5-(and-6)-carboxy SNARF-1 (SNARF). The pH was determined by ratiometric measurement of the fluorescence of SNARF at emission wavelengths of 582 and 698 nm (Fig. 2F) or by nonratiometric measurement at an emission wavelength range of 605 to 660 nm based on the microscopic setup used for signal readout (fig. S2). We ensured that the pH gradient extended to the full range of the inlet values of pH 7.4 and 6.0 despite the high diffusion constant of the hydronium ions (H_3O^+, the form in which H^+ will diffuse in aqueous solution) by applying a sufficiently high flow velocity of 8.35×10^{-3} m/s and keeping the Peclet number high (900), preventing diffusion from washing-out the gradient within the observation area (Fig. 2, G and H). The shape of the gradient produced in the mixing device depended on the flow rate and was hence sensitive to the formation of air bubbles. Therefore, we included an air trap (*26*) to suppress air bubbles (fig. S1). In addition, we controlled the liquid flow with fixed flow rates rather than a constant pressure to avoid factors such as hydrostatic pressure in connection tubing that could influence the pressure distribution in the microfluidic device and thus the gradient profile in the observation area. These results demonstrate the successful implementation of a microfluidic device, which can produce a stable pH gradient from pH 7.4 to 6.0 over a 5-mm distance in a 150-μm-thick collagen I layer.

Live imaging of cell motility and directionality in a pH_e gradient

Chemotaxis and chemokinesis are the movement of cells in a given direction or with a given speed, respectively, dictated by specific signaling gradients. Cells express bona fide proton sensing receptors that could direct such behaviors (*27*), and "pH taxis" is well established in bacteria (*28*). We and others have shown extra- and intracellular pH (pH_e and pH_i, respectively) to regulate mammalian cell migration (*29*, *30*), but the role of pH as a chemotactic signal in mammalian cells is not understood, with the few available studies providing contradictory results (*31*, *32*).

To demonstrate the utility of our device for studying chemotaxis and chemokinesis, we embedded MDA-MB-231 human breast cancer cells in the collagen I layer at a concentration of 4×10^6 cells/ml. We assembled the device, established a pH_e 7.4 to 6.0 gradient using CO_2/HCO_3^--buffered media in the 5% CO_2 atmosphere of the environmentally controlled microscope chamber, and performed bright-field imaging of 5-μm step z-stacks of 1400 × 1400 pixels over 4 hours in time intervals of 10 min. Imaging was performed at five positions along the pH gradient (Fig. 3A). At each of these positions, we imaged three regions along the *y* axis as technical replicates, since there is no pH gradient along this axis. After mean intensity projection to enable the visualization of all cells in each z-stack in a single projection, the cells were identified using Cellpose (*33*), a machine learning method, tracked using the Fiji plugin TrackMate (*34*), and further analyzed by subtracting the stage drift from the single-cell trajectories (Fig. 3B). Examples of single-cell trajectories from a pH 6.0 region (Fig. 3C, left) and a pH 7.4 region (Fig. 3C, right), normalized to a common starting point, are shown, illustrating that the displacement was much smaller at the lower pH_e values (i.e., reduced chemokinesis at acidic pH_e), whereas we did not observe "pH"-tactic behavior (directional movement in the direction of the pH gradient) (Fig. 3C). To visualize this across the gradient, we plotted the step size per 10-min interval at each position, in three independent experiments (Fig. 3D). At higher pH_e values (7.4), we observed a tendency for step size to decrease again from position 4 to position 5 (Fig. 3D). This, as well as the reduced short-term displacement at a low pH_e occurring within hours, is consistent with previous reports, where it was attributed to increased cell-matrix adhesion at low pH_e and reduced adhesion at higher pH_e values (*29*). Notably, this short-term effect is different from the long-term (weeks and months) effects of cancer cell growth in an acidic environment, which generally increases motility and invasiveness (*5*).

In summary, we designed a workflow for the label-free imaging and tracking of the speed and *x*-*y* displacement of cells in a pH gradient. Over the short time frame used, the displacement speed of MDA-MB-231 cells decreased with decreasing pH_e in the range of pH_e 7.4 to 6.0.

Analysis of cell viability, proliferation, and apoptosis across the pH gradient

There is a close, albeit cell type–dependent, coupling between pH_e and pH_i in mammalian cells which can be expected to result in gradually reduced pH_i along the pH_e 7.4 to 6.0 gradient (*35*). Given the impact of pH_i on cell proliferation and death/survival balance (*36*, *37*), one could therefore expect to see differences in these parameters along a pH gradient. To test the sensitivity of the system, we subjected the MDA-MB-231 cells to the pH_e gradient for only 4 hours. We exploited that the microfluidic device can be reopened after application of the pH gradient (Fig. 4A) and opened the device after 4 hours to study the cells using live/dead staining and IF analysis. In both cases, imaging was performed as above at five positions along the pH gradient but with four to five replicates along the *y* axis (Fig. 4B).

We first assessed cell viability by live/dead staining with calcein-acetoxymethylester (AM) and propidium iodide (PI), followed by epifluorescence imaging (exemplified in Fig. 4C) and quantification using the Fiji software (Fig. 4D). Our results revealed that MDA-MB-231 cell viability was not affected by the pH_e gradient. To further dissect the impact of the pH gradient, we fixed the cells with p-formaldehyde and applied standard IF analysis protocols, using Ki-67 as a marker for proliferation, and cleaved poly(ADP-ribose)polymerase-1 (PARP-1) as a marker for apoptosis (Fig. 4, E to G). PARP-1 cleavage was only detected in a small fraction of the cells, consistent with the lack of change in total viability. However, our data indicated a gradient of decreasing PARP-1 cleavage, i.e., decreased apoptosis, with decreasing pH_e (Fig. 4F). This suggests that short-term moderate pH stress does not cause apoptotic cell death. Similarly, Ki-67 staining did not indicate that proliferation differs systematically across the gradient within the 4-hour time course of the experiment (Fig. 4G).

These results demonstrate another key design feature of the device: It can be reopened without damage to the cells in the collagen layer, allowing for functional assays requiring procedures beyond optical

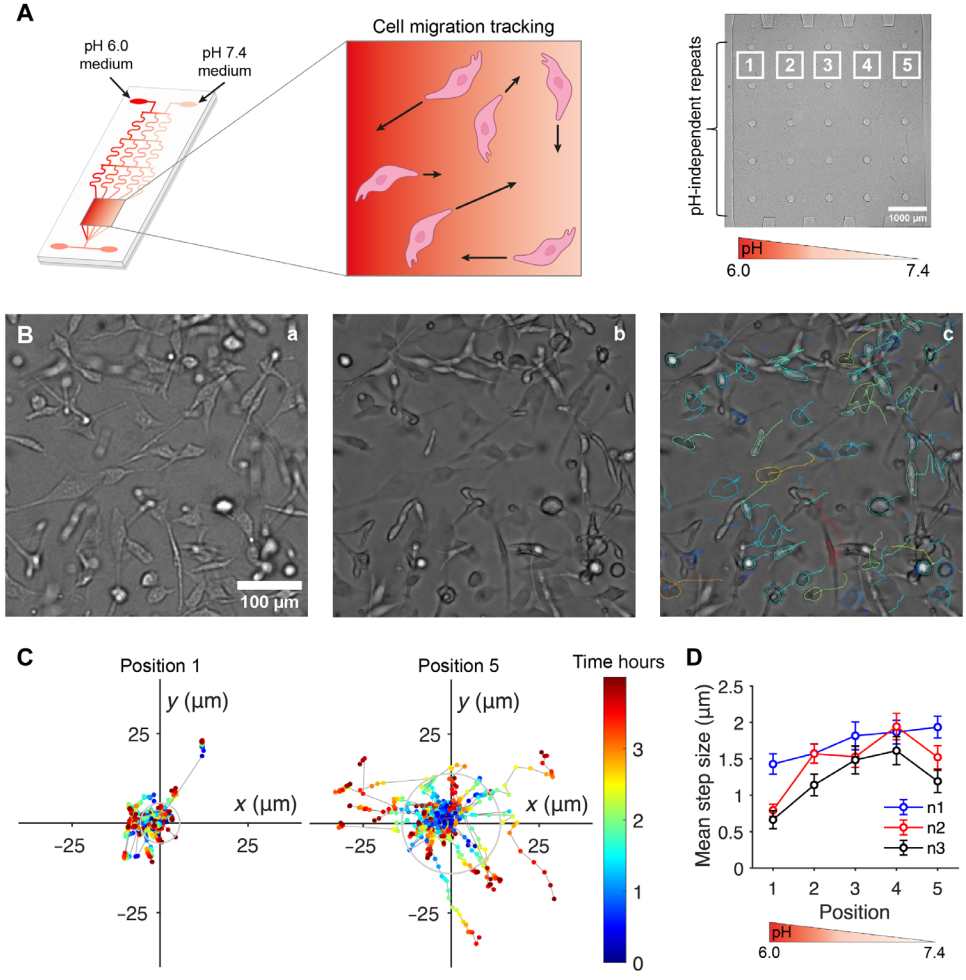

Fig. 3. In situ gradient characterization and cell migration study. (**A**) Overview of the experimental setup and the imaging positions for cell migration analysis. Images were taken in five different positions along the gradient axis, in three different gradient areas. (**B**) Example of MDA-MB-231 cell tracking and image processing in three steps: (B-a) z-stacks (5-µm steps, 25 slices) were taken in bright-field mode in each position, every 10 min for 4 hours. (B-b) Average intensity projections were obtained for each z-stack using ImageJ, resulting in a movie for the 4-hour experiment. (B-c) Cells were identified using Cellpose (*33*), after a manual training on 10 images, starting with the cyto pretrained model, and tracked using the TrackMate plugin in Fiji. (**C**) The pseudo-colored tracks show the movement of individual cells over time, corrected for stage drift and the cell starting position: For each cell, at each time point (shown as dots), the coordinates are corrected for stage drift and normalized to the coordinates of the first occurrence of the cell. The *x* axis represents the distance along the gradient, and the *y* axis represents the distance along the flow. The color scale bar shows time in hours. Lines represent the cell tracks, and the circle represents the mean translocation. (**D**) For each position in the gradient, step sizes (distance traveled by the cell from one time point to the next) are calculated, and the average step sizes (approximately 30 cells per position, SEM error bars) are plotted against positions 1 to 5 (pH 6.0 to pH 7.4). The data in (D) represent three independent biological replicates, each with three to five technical replicates.

imaging, such as live cell staining and IF analysis. Furthermore, we demonstrated that even a short period of culture in a pH_e gradient from 7.4 to 6.0 results in a detectable gradient of apoptosis, which is consistent with previous data obtained in 2D (fig. S3).

Extraction of RNA from cells within the observation chamber for spatial transcriptomics analyses

To enable the measurement of mRNA levels across the cells subjected to the pH gradient in the microfluidic device, we designed the dimensions of the observation area and the corresponding collagen I/cell layer to match the capture area of the 10x Genomics Visum GEX slide for spatial transcriptomic analysis [reviewed in (*24*)]. Briefly, the Visium GEX platform allows for profile gene expression of 5- to 35-µm-thick frozen tissue sections, which are permeabilized on a capture area composed of a glass slide printed with an array of ~5000 oligonucleotide spots. Each spot contains 82-nt-long single-stranded DNA oligonucleotides with the following features: a poly(dT) region to capture mRNA polyA tails, a 12-nt unique molecular identifier (UMI), a 16-nt spatial barcode specific for the spot, and a partial Illumina TruSeq Read 1 sequence. Once the cells in the tissue are permeabilized, mRNAs diffuse to the capture spots and hybridize with the oligonucleotides where they are subsequently converted to double-stranded cDNAs. The second-strand cDNA is released from the glass slide, subsequently fragmented, indexed, amplified, and lastly sequenced using an Illumina platform. Each cDNA contains a spatial barcode to enable the calculation of cDNA abundance at specific spatial locations in the original tissue slide upon sequencing.

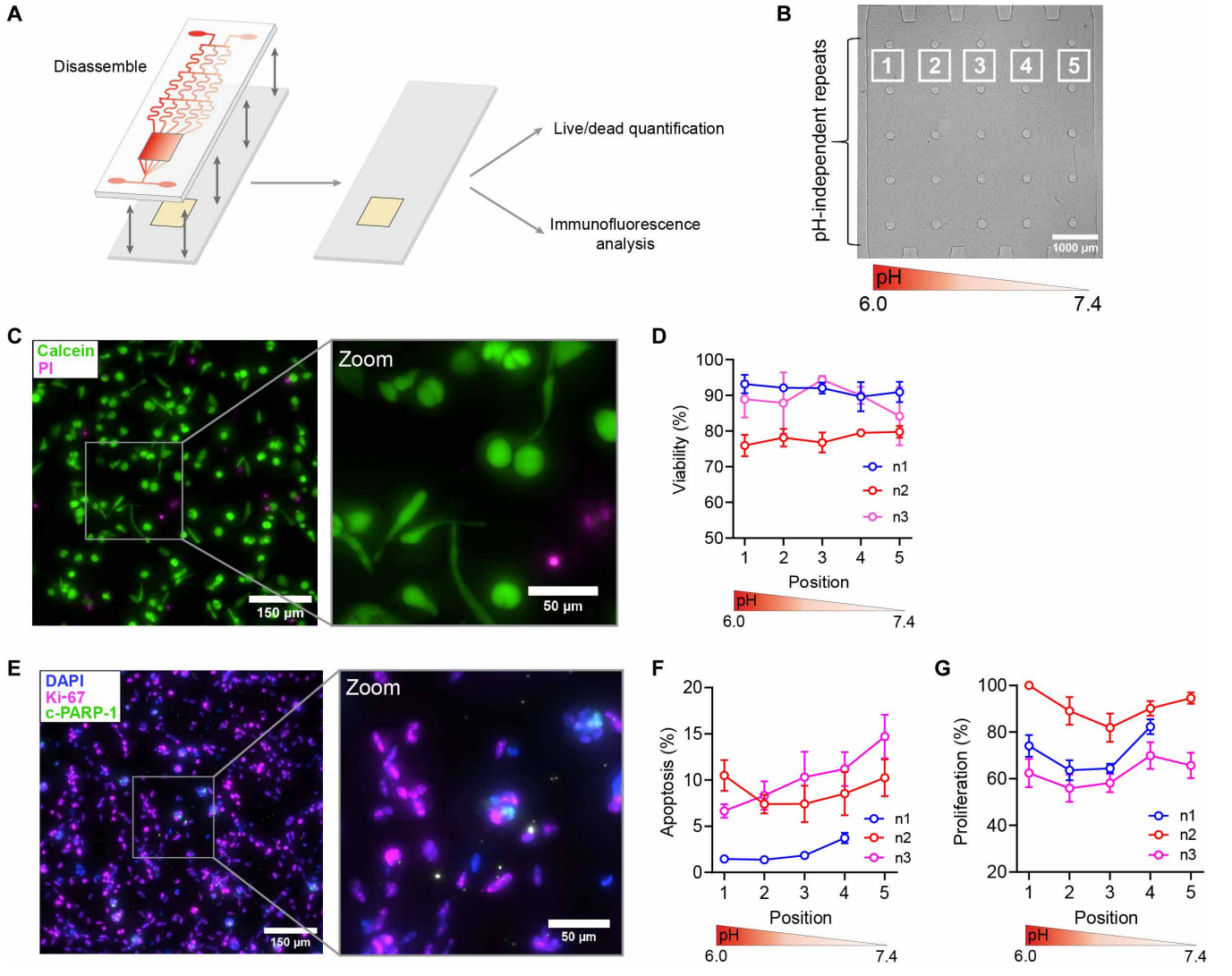

Fig. 4. Effect of the pH gradient on cell viability and proliferation and apoptosis markers. (**A**) Schematic showing the opening of the device. (**B**) Photo of the gradient area, showing the position of the imaged regions across the pH gradient (left-right). Note that this is the same image used in Fig. 3A, shown here to illustrate the setup. (**C**) Merged fluorescence image (left) and zoom (right) of MDA-MB-231 cells stained with calcein-AM (3 μM, live cells) and propidium iodide (PI; 3 μM, dead cells). Calcein and PI fluorescence were excited at 488 and 575 nm, respectively. (**D**) Quantification of data as in (C) along the pH gradient. Data from three independent biological experiments, SEM error bars for technical repeats [along the top-bottom axis as shown in (B)]. (**E**) MDA-MB-231 cells stained for KI-67 (proliferation), cleaved PARP-1 (c-PARP-1) (apoptosis), and 4′,6-diamidino-2-phenylindole (DAPI; nuclei). Merged fluorescence image (left) and corresponding zoomed image (right) of cleaved PARP-1 (green), Ki-67 (magenta), and DAPI (blue) fluorescence. The percentage of stained cells quantified for each channel using ImageJ is shown in (F) (cleaved PARP, apoptosis) and (G) [Ki-67, proliferation (actively cycling cells)]. (**F** and **G**) Data from three independent biological repeats, with SEM error bars for the three to five technical repeats in each biological repeat.

For the use in our device, we developed a protocol enabling the capture of the thicker (150 μm) collagen I/cell layer corresponding to the pH gradient region (Fig. 5A). Therefore, the collagen I/cell layer was methanol-fixed and embedded in optimal cutting temperature (OCT) compound (Fig. 5, A and B). To ensure the application of the optimal amount of OCT for the freezing the layer into a block and allowing its detachment from the microfluidic slide, a 250-μm-thick precut silicone membrane was placed around the collagen I/cell layer before addition of the OCT on top of the layer. The poly-L-lysine (PLL) glass slide was transferred to an aluminum cooler block chilled on dry ice, and a new glass slide was immediately placed on top to flatten the OCT to snap freeze into an OCT/collagen I block. The setup was disassembled, and the frozen OCT/collagen I block was detached from the PLL glass slide. This frozen OCT/collagen I block was lastly transferred to the capture area on the Visium slide, and the OCT was rinsed off with phosphate-buffered saline (PBS).

This method was designed to transfer the full collagen I/cell layer, keeping the original structure, minimizing impact on RNA integrity, and allowing spatial capture of RNA. To investigate the impact of OCT-based treatment on cell morphology, the collagen I/cell layer was either fixed with methanol (control condition) or fixed with methanol and treated with OCT before hematoxylin and eosin (H&E)

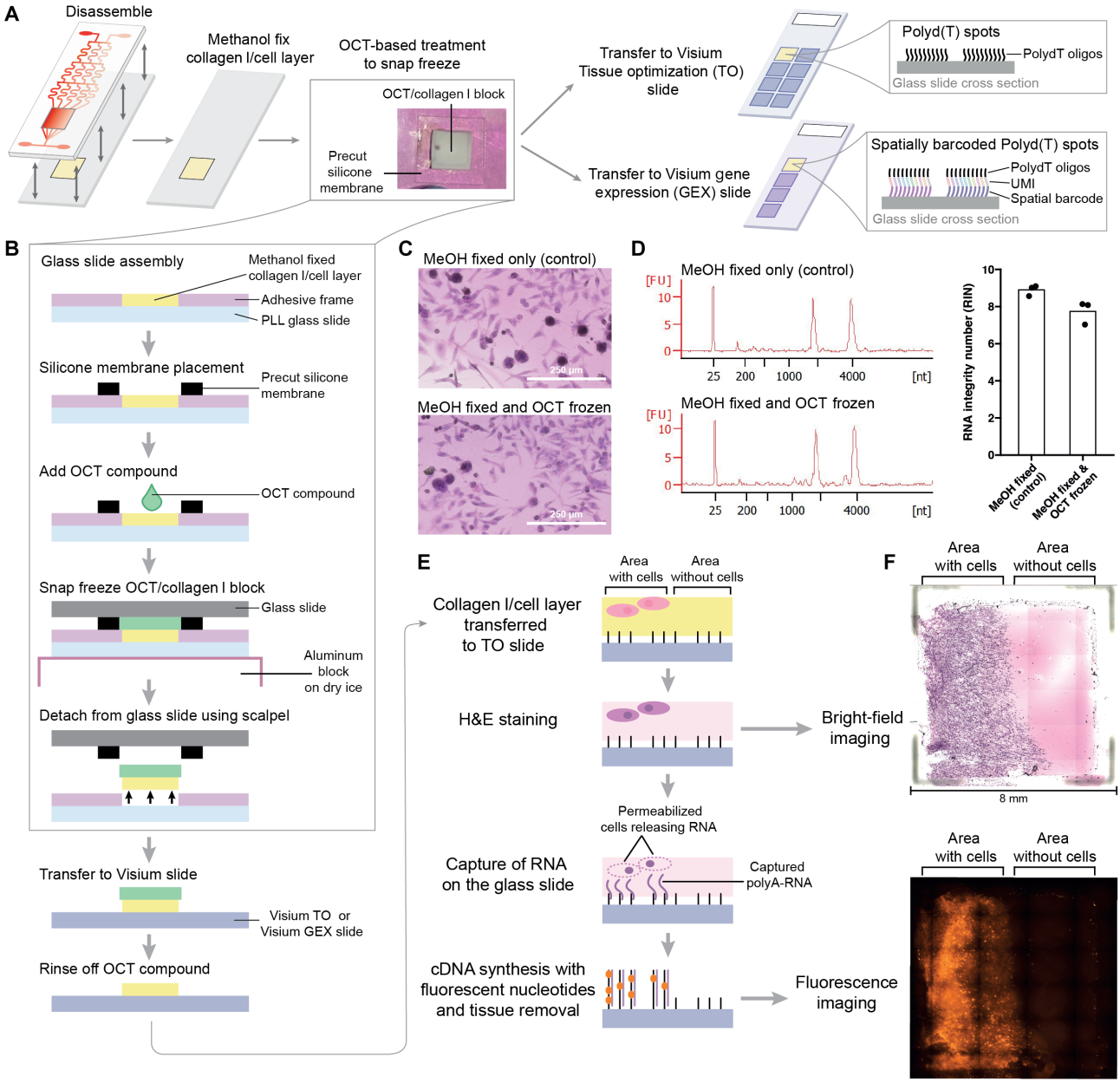

Fig. 5. Transfer of the cells in collagen I layer from the microfluidic device to a Visum capture area followed by spatially resolved RNA capture. (**A**) Schematic overview showing the collagen I/cell layer transfer to Visium slides. (**B**) Detailed process flow for the OCT-based treatment and transfer of collagen I/cell layer. (**C**) H&E-stained images of collagen I/cell layers that were either methanol fixed only (control) or methanol fixed and frozen in OCT to determine the effect of OCT-based treatment on cell morphology. (**D**) Effect of the OCT-based treatment on RNA integrity. On the left are bioanalyzer electropherograms of RNA extracted from collagen I/cell layers methanol fixed only (control) or methanol fixed and frozen in OCT. The *x* axis is the RNA length (nt), and the *y* axis shows the fluorescence units (FU), where the fluorescence measured correlates with RNA amount of a given size. The bar plot on the right summarizes the RNA integrity number (RIN) values of RNA extracts from each condition using three replicates per condition. Bar height shows the mean across all three technical replicates: Dots show individual replicates. (**E**) Detailed process flow for spatial RNA capture validation using the Visium TO slide. (**F**) On the top is a stitched bright-field image of a patterned collagen I/cell layer transferred onto a Visium TO slide then stained with H&E. On the bottom is a stitched fluorescence image of the same collagen I/cell layer after permeabilization, cDNA synthesis, and tissue removal. Dark areas on the border between adjacent tiles on the fluorescence image are due to stitching artifacts from the imaging system. MeOH, methanol.

staining (Materials and Methods, the "Morphology and RNA quality control from cells in OCT/collagen I blocks" section). Our data reveal that under both conditions, the H&E-stained collagen I/cell layers showed intact cells, demonstrating that OCT treatment does not affect cell morphology (Fig. 5C). To explore the impact of the OCT-based treatment on RNA integrity, RNA extracted from a fixed, OCT-frozen collagen I/cell layer prepared as described above was compared to measurements of RNA extracted from a similar sample that was fixed but not frozen in OCT (control) (Materials and Methods, the "Morphology and RNA quality control from cells in OCT/collagen I blocks" section). Pico bioanalyzer analysis showed similar RNA length distributions between samples with sharp ribosomal

RNA (rRNA) bands for 28*S* and 18*S* rRNA (Fig. 5D, left), and RNA integrity numbers were 7 or above for both RNA samples (Fig. 5D, right). Thus, RNA quality is not compromised by the OCT treatment, and the extracted RNA is suitable for the subsequent preparation of a library.

To determine the extent of lateral diffusion of RNA within the collagen I/cell layer upon cell permeabilization, we created a patterned collagen I/cell layer, where only half of the layer contained cells (Materials and Methods, the "Cell lines and culture conditions" section). We transferred this layer using the previously described approach, followed by cell permeabilization and hybridization of the extracted RNA to a Visum tissue optimization (TO) slide—a Visium slide sharing the same properties as the normal Visium GEX slide except that spots containing the polyd(T) oligonucleotides do not contain spatial barcodes (Fig. 5E and Materials and Methods, the "Modified Visium TO method" section). After cDNA synthesis of captured RNA using labeled nucleotides, fluorescence imaging showed minimal RNA associated with the cell-free region and clearly defined signal borders corresponding to the cell border in the original patterned collagen I/cell layer. This provides evidence for minimal lateral diffusion (Fig. 5F).

Overall, these results indicate that our method is suitable for the transfer of the full collagen I/cell layer to a Visum capture slide while retaining the original structure, allowing spatial capture of RNA with high integrity scores and small lateral diffusion.

Identification of pH-regulated genes by spatial transcriptomics

To demonstrate the use of our microfluidic workflow for profiling gene expression across a pH gradient, we subjected MDA-MB-231 cells to a pH_e 7.4 to 6.0 gradient in the microfluidic device for 4 hours. The experiments were done in triplicate, using three independent devices run in parallel (Fig. 6A). Using the same protocol as described before, we transferred the frozen collagen I/cell blocks to three capture areas of a Visium GEX slide, extracted RNA, and converted the captured mRNAs to cDNA (Materials and Methods, the "Modified Visium spatial GEX

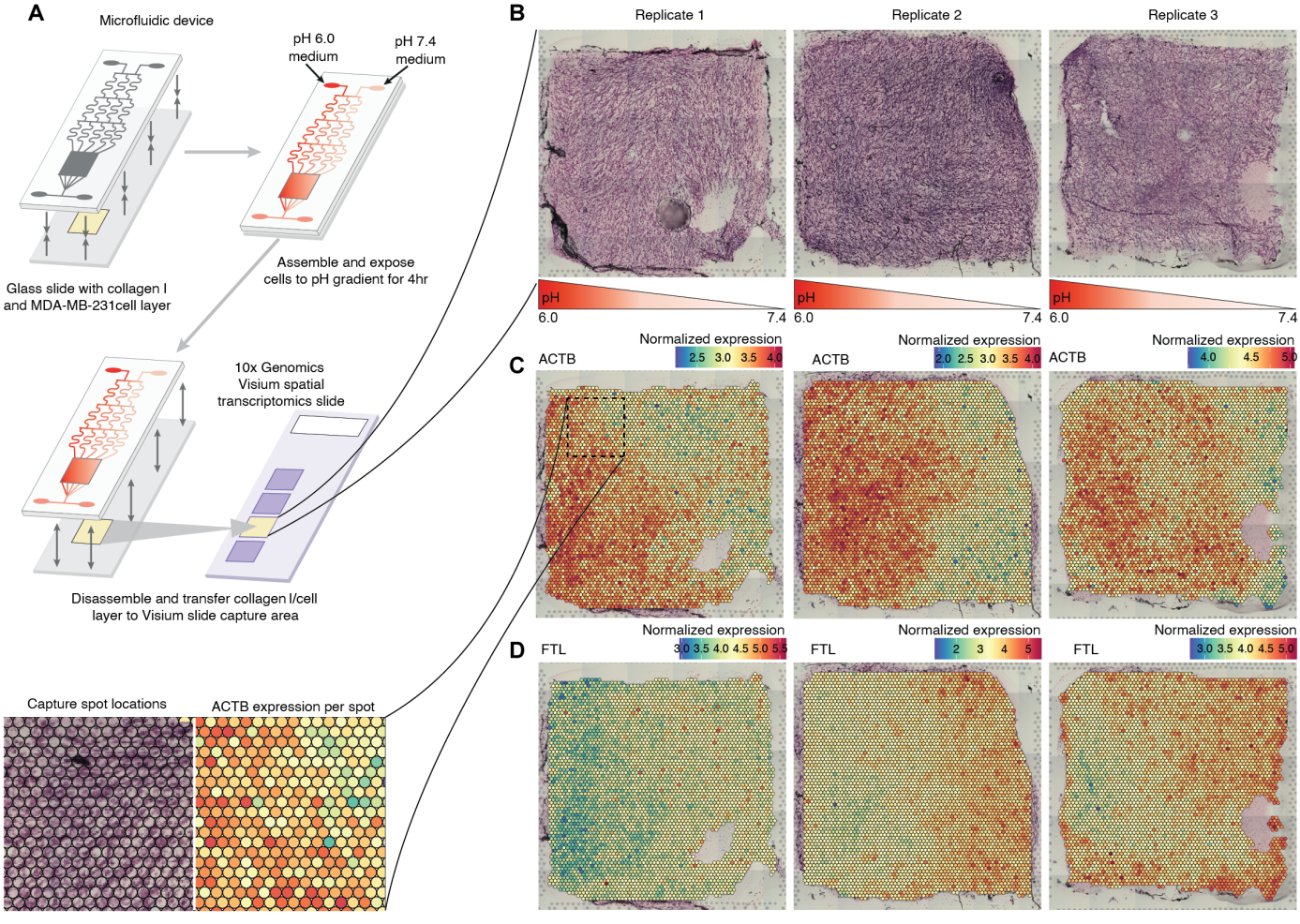

Fig. 6. Measuring gene expression changes across the pH gradient using spatial transcriptomics. (**A**) Overview of experiment. MDA-MB 231 cells were exposed to a 6.0 to 7.4 pH_e gradient for 4 hours. The collagen I/cell layer was transferred to a capture area of a Visium GEX slide, using three replicates with independent devices in parallel. (**B**) Photos of Visum capture areas with transferred collagen I/cell layers. *X* axis corresponds to the pH gradient. Each photo is one replicate. (**C**) Spatial expression of *ACTB1*. Images show expression from respective collagen I/cell layer in (B). Hexagons correspond Visium capture spots, and color indicates normalized expression. A zoom in of an area in the Visium GEX slide is shown: The left part shows Visium capture spots overlaid on the transferred collagen I/cell layer, and the right part shows the same image overlaid by ACTB1 expression. (**D**) Spatial expression of *FTL*. The image is organized as in (C) but shows *FTL* expression in the same Visium slides.

method" section). Released cDNAs were sequenced using the Illumina NovaSeq platform with an average sequencing depth of 477 million read pairs per library. UMI counts of mRNA sequences were estimated using Space Ranger and log-normalized using Seurat (*38*). Fractions of mitochondrial gene counts are often used as an estimate for overall quality, with high fractions indicating many dead cells. In our system, the average fraction per capture spot was 0.07 to 0.12, and only a handful of spots had fractions >0.20, a common quality threshold (fig. S5A). Figure 6B shows the collagen I/cell layer placed on Visum GEX capture areas, while Fig. 6 (C and D) shows two examples of spatially resolved normalized expression patterns across the pH gradient originating from the same samples: *ACTB1*, coding for the ubiquitous β-actin protein, showed a clear correlation between high expression and low pH, while *FTL*, coding for the light chain of ferritin, the major cellular iron storage protein, showed the opposite pattern.

To identify common patterns of expression as a function of pH, we binned each Visium capture area into 50 by 50 bins, calculated the median expression of each the 50 vertical bins at each x coordinate, and then clustered these vectors of medians using hierarchical clustering (fig. S5B). A total of 233 highly expressed (average count per spot > 1), reproducible (average correlation of expression across 3 samples > 0.05), pH-dependent [maximal information coefficient (MIC) > 0.1] genes were used as input of the clustering. This showed that for most genes, expression changes were gradual and monotonic functions of pH, exemplified by *CISD2* and *TNIP1* (fig. S5C). On the basis of these results, we used a cutoff based on MIC–Pearson's R^2 (*39*) to establish that the expression of 94% (219 in 233) of investigated genes had a linear relationship with pH (Materials and Methods, the "Visium spatial GEX data processing" section). The 14 genes not following a linear relationship with pH showed diverse expression trajectories, for example, (i) multimodal expression patterns where the highest expression was observed at both the lowest and highest pH values, exemplified by *MT-CYB* (fig. S5C) and 9ii) trajectories where the highest expression was observed somewhere between the highest and lowest pH, exemplified by *CCN1* (fig. S5C). Notably, subsets of genes whose expression was classified as a linear function of pH showed an initial expression increase, followed by nonchanging expression levels when assessing low to high pH, as exemplified by *SIVA1*, or vice versa, as exemplified by *NEAT1* (fig. S5C).

Because monotonic increase or decrease of expression across all measured pH was the most common response, for the rest of the analysis, we modeled gene expression abundance as a function of x-axis positions as a linear model for each gene in each Visum GEX capture area. The t_x statistic in the model estimate describes the relation between the x-axis value and gene expression. Positive t_x values indicate that gene expression increases with increasing pH_e (i.e., gene expression decreases in acidosis), while negative t_x values imply that gene expression increases with decreasing pH_e (i.e., increases with acidosis). Overall, gene t_x values were substantially correlated between replicates (Pearson's $R = 0.46$ to 0.68; fig. S5D). We found 318 genes whose t_x values were >7 or <−7 and consistent between replicates: The t_x values of these genes are shown in Fig. 7A, and their average expression patterns across the y axis as a function of x-axis position are displayed in Fig. 7B. To more generally assess functions of these, we first made STRING database (*40*) plots of the genes with average $t_x > 7$ or <−7 in the heatmap [Fig. 7C; full plots in fig. S5 (E and F)].

Next, we performed gene set enrichment analysis [Gene Ontology terms or Kyoto Encyclopedia of Genes and Genomes (KEGG) pathways (*41*)] based on the ranking of all genes by the average t_x value across replicates (Fig. 7D shows selected terms; full results in table S2). Both analyses showed strong patterns:

First, genes with low t_x values (i.e., gene expression increasing with acidosis) were functionally diverse (Fig. 7D) but highly linked (Fig. 7C) and associated with four major functional themes:

1) Cytoskeleton organization, including microtubules (e.g., *TUBB* and *TUBA1C*), cytoskeleton anchoring (*ACTN4* and *EZR*), and cell migration (e.g., *MYH9* and *ACTG1*). This is consistent with previous reports showing that pH_e substantially affects cell migration and invasion (*5*, *8*, *29*).

2) Negative regulation of apoptotic process: A diverse set of genes associated with inhibiting or limiting the extent of cell death by apoptosis were in this group, including *TP53*, a well-known tumor suppressor, *BCL2L1*, an inhibitor of cell death, and *BIRC3* and *BIRC5* which are inhibitors and/or modulators of apoptosis. This is likely part of a stress response induced by the exposure to acidic conditions and fully in line with the increased resistance to cell death observed in cancer cells adapted to the acidic TME (*5*). It is also consistent with the observed gradient of decreased apoptosis with low pH_e (Fig. 4G) in the present work, although we did not establish causality.

3) Response to oxygen-containing compound: Both hypoxia-inducible factor 1A (*HIF1A*) and thioredoxin-interacting protein (*TXNIP*) were up-regulated with increasing acidosis. While mostly regulated at the level of protein degradation, HIF1A has been shown to be up-regulated by acidosis (*42*, *43*). Our data reveal that this transcription factor, which plays essential roles in cancer development, is highly sensitive to acidosis also at the transcriptional level. TXNIP is a key regulator of cellular metabolism and redox state, and we and others have previously shown TXNIP to be substantially up-regulated by acidosis and in acid-adapted cancer cells (*9*, *44*). Using our microfluidic workflow, we can now show that *TXNIP* gene expression is a highly sensitive function of pH, detectable after only a few hours in the pH_e gradient.

4) RNA metabolic genes, dominated by ribonucleoproteins with diverse RNA binding roles, including RNA splicing, transport, stability, and chromatin-associated RNAs. As this is a generic function group, it is difficult to directly functionally associate it with the pH gradient.

Second, genes with high t_x values (gene expression increasing with increasing pH, i.e., decreasing with acidosis) were dominated by two large and two smaller functional groups:

1) A large cluster of highly connected ribosomal protein genes, from the large and small ribosomal subunits (*RPS* and *RPL* genes) as well as from the mitochondrial ribosome (*MRP* genes). An increase of ribosome gene production is often associated with an increased protein production capacity and, in turn, cell growth (*45*). Hence, these data are consistent with the known inhibition of protein synthesis at low pH (*36*).

2) A large cluster encompassing oxidative phosphorylation genes, including cytochrome oxidase subunit genes (e.g., *COX5A2*, *COX7B*, and *COX6C*), NADH (reduced form of nicotinamide adenine dinucleotide) dehydrogenase subunit genes (e.g., *NDUFB*3, *NDUFB4*, and *NDUFB6*), and F1F0 adenosine triphosphate synthase subunit genes (e.g., *ATP5PF* and *ATP5MC3*). The reduced expression of these genes in the first hours after exposure to acidic conditions was unexpected as we and others have previously observed an increase in preference for oxidative phosphorylation in cells adapted to growth under acidic conditions (*9*). However, scrutinizing RNA sequencing data for such long-term adapted cells showed a similar decrease in many of these

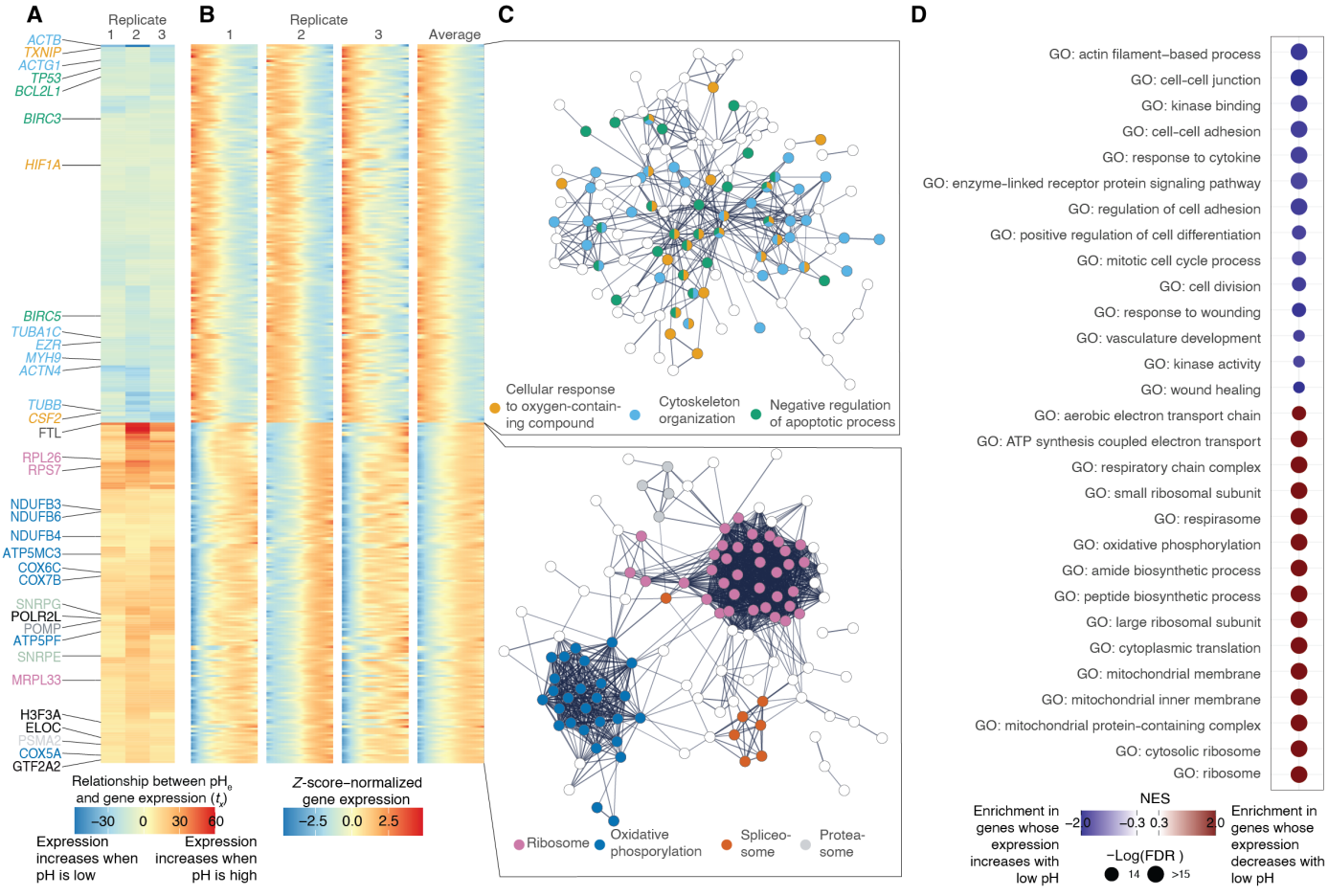

Fig. 7. Analysis of spatial gene expression changes across the pH gradient. (**A**) Identification of genes whose expression correlates with the pH gradient. Rows show 318 genes with high correlation between expression and pH ($|t_x| > 7$) were selected (see Materials and Methods); top and bottom rows show with high (>7) and low t_x values (<−7). Genes discussed in the main text are highlighted, with colors corresponding to functional classes in (C). Columns show replicates, and colors indicate t_x values. (**B**) Row shows genes as in (A). The first three columns show replicates, and the last shows the average of the replicates. For each replicate, the *x* axis in the Visum GEX slide data is summarized into 100 bins, and the average expression across the *y* axis in the replicate is calculated. Each row is then *z*-score–normalized, indicated by color. (**C**) STRING plots for genes in (A) and (B). Dots indicate genes/proteins, colored by selected GO terms. Only high confidence interactions are shown; line show strength of interaction evidence is. Nonconnected genes/proteins are not shown. (**D**) Gene set enrichment analysis based on average t_x value ranking. Gene sets enriched in genes having low or high t_x scores are shown as rows. Dot color indicates normalized enrichment, and sizes indicate significance −log[false discovery rate (FDR)]. See table S2 for full analysis results. ATP, adenosine triphosphate; NES, normalized enrichment score.

genes in MDA-MB-231 cells [see supplementary data tables in (*46*)], revealing a clear difference between the changes in mitochondrial gene expression and function under acidic stress.

3) Two smaller clusters consisting of spliceosomal (e.g., *SNRPE* and *SNRPG*) and proteasomal genes (e.g., *PSMA2* and *POMP*) likely connected to reduced protein production at lower pH, as discussed above. Related to this, we also observed that the general transcription factor, histone, RNA polymerase, and RNA elongation genes (e.g., *GTFA2*, *POLR2L*, *H3F3A*, and *ELOC*) share the same pattern.

Because the device is designed to produce invariant pH values across the *y* axis in the observation chamber, gene expression should not systematically increase or decrease along the *y* axis. We investigated this in two ways. First, we modeled gene expression as a function of *y*-axis position, defining a t_y estimate for each slide and gene, analogous to our analysis above estimating t_x. The t_y values were substantially closer to 0 than the t_x values (fig. S5G). Using the same thresholds as done before when analyzing t_x, not a single gene had a high and consistent change across the *y* axis ($|t_y| > 7$ in all replicates), as opposed to 318 genes on the *x* axis. Second, plotting average t_x versus average t_y values showed that the *y*-axis contribution to gene expression was overall minor (fig. S5H).

These results demonstrate the feasibility of combining the microfluidic device with spatial transcriptomic analysis of gene expression gradients. Furthermore, we could show that the regulation of key genes previously identified to be regulated in cancer cells by acidic pH can be detected as monotonic expression functions of pH after only 4 hours. Corresponding changes in protein levels are slower than the 4 hours studied here for many genes. Therefore, the observed phenotypic changes shown in Figs. 2 and 3 may not have manifested in this shorter-term experiment. However, our data illustrate how rapidly and sensitively genes respond to pH$_e$ and open new roads for the understanding of the early response to extracellular acidosis.

DISCUSSION

In this study, we designed a complete, integrated workflow for imposing microenvironmental gradients on mammalian cells freely moving in a 3D matrix and validated its performance. Our workflow allows studying the impact of such gradients on a range of cell phenotypes, including cell motility and chemotaxis, cell viability, proliferation and apoptosis, and gene expression levels, maintaining highly resolved spatial information. The workflow is highly versatile, as it allows for both continuous imaging of cell behaviors and terminal analyses that require access to cells, such as IF analyses and genomics assays.

In our workflow, cells are deposited using a collagen matrix because this is physiologically relevant. However, the device would also work if the cells were seeded in 2D on a solid surface. Others have done this, albeit not in a pH gradient, by seeding cells inside a closed microfluidic device [e.g., (*18*, *19*)]. Using a gel allows one to proceed immediately to the gradient experiment without the delay of culturing cells inside the device, to reversibly close the device without the cells disturbing the sealing, to reopen the device while keeping the cells in place, and to integrate with the spatial transcriptomics workflow. Note that in the case where cells are seeded on the surface of the microfluidic device, they are exposed to the shear stress from the liquid flow, which may or may not be wanted. Using a gel matrix implies that the pH gradient is imposed to the cells by diffusion through the gel. Because the depth of the gel (150 μm) is almost an order of magnitude smaller than the width of the pH "lanes" in the gradient (about 1 mm), the pH in the gel equilibrates with solution within a minute and matches the pH in solution throughout the whole gel depth (fig. S6). Our resealable device ensures that the microfluidic PDMS device is reusable.

The main novelty of our workflow is that it integrates microfluidic modeling of TME parameters with a design that can be used for live imaging, reopened and subjected to spatial transcriptomics. In this context, several methods were developed that will be relevant also in other contexts than our workflow, including the adaptation of the Visium methodology developed for tissues to a 3D cell–collagen I layer. Because the system is modular, it can be further developed in multiple ways. Here, we demonstrated its use and applicability for generating a pH gradient. However, the microfluidic mixer system can easily be adapted to gradients of other parameters of physiological interest, such as lactate, cytokines, or other nutrients and signaling molecules. Further adaptation to gaseous gradients, such as oxygen, is also principally feasible exploiting the permeability of PDMS to gases such as oxygen. This will only require the incorporation of gas channels adjacent to the media channels. Because of the physiological conditions, i.e., temperature-controlled 3D growth in CO_2/HCO_3^- buffered medium, the workflow is amenable to long-term experiments. Furthermore, while available microfluidic devices focus on spatially rather than temporally modulated gradients, our device can also easily be used to study the impact of oscillatory changes in concentrations of small molecules, because the device allows precisely controlled spatiotemporal changes to the gradient. This would, for instance, be highly interesting for oscillatory changes in pH such as those occurring postprandially in the stomach or pancreatic duct interstitium (*47*). In addition, this device can be used for the coculturing of multiple cell types, e.g., for addressing research questions such as how cancer cells and immune cells interact in microenvironmental gradients in tumors. In this case, the collagen I layer used here can be replaced by Matrigel or other extracellular matrices of choice. Another elegant application is the combination of genetically encoded sensors for, e.g., pH, lactate, and hypoxia, thereby obtaining valuable information about the cellular response to the gradients in real time and with high resolution. The information that can be gained from studying cellular responses in a continuous gradient extends much beyond studies in discontinuous systems, with chemotactic behavior as an obvious example requiring the application of a gradient. However, it is worth noting the convenience of our gradient system compared to, for instance, trying to obtain protein localization or gene expression data from a 96- or 384-well plate with a range of different pH values. The spatial transcriptomics workflow present here should also enable the combination with next-generation platforms that allow for single-cell or subcellular resolution (*48*), which is particularly advantageous for the simultaneous study of multiple cell types and their interactions.

The data obtained here by using our workflow are in their own right of great biological interest and novelty. We show here that a short exposure, only 4 hours, to a pH_e gradient from 7.4 to 6.0 can generate clear gradients of expression of numerous genes, illustrating the exquisite sensitivity of many genes to pH_e. For instance, we show that TXNIP, a major regulator of cellular metabolism and redox homeostasis (*49*), is strongly up-regulated in this short time frame, in a manner correlating with the pH gradient. While the time frame used here is likely too short for observing major changes in the expression of most proteins, additional levels of information could be obtained especially in experiments run on a longer timescale, by replacing the transcriptomics step with spatial proteomics or even combining these with multiomics approaches (*50*). Functionally, we showed that cell migration speed was reduced at low pH_e. This is qualitatively consistent with previous reports (*29*), but by combining the pH_e gradient with machine learning and single-cell tracking in a 3D matrix, our workflow enables much more detailed and in-depth analysis. In contrast, the MDA-MB-231 cells did not exhibit detectable pH-tactic behavior. Another innovative use of our workflow would be to interrogate how pH gradients in the TME affect directional migration of pro- and antitumorigenic immune cells, which have been shown to be sensitive to tumor pH_e [reviewed in (*35*)] or to exploit coculture models of cancer and immune cells to study how pH_e gradients affect cell-cell communication. The fraction of apoptotic cells declined with increasing acidosis, indicating that limited acidosis may exert an anti-apoptotic effect in this setting. This is reminiscent of what has been demonstrated in the context of cardiac ischemia (*51*) and could contribute to the exacerbation of cancer hallmarks in the TME.

Our workflow is not without limitations. It is, for instance, not yet inherently a high-throughput setup. However, multiple devices can be run in parallel, dependent on the experimental design and microscope platform. It is also subject to the general limitations of the individual techniques. For instance, the spatial resolution of the Visium GEX slide is not compatible with single-cell–level analysis, and therefore, expansion of the system to multicell coculture will require a change of spatial transcriptomics technique.

Future developments will include the expansion to profiling multiple gradients at the same time. For instance, one goal is to combine gradients of lactate, pH, and oxygen, which will be of particular interest for mimicking the TME (*5*). This, in combination with the above-mentioned increase in spatial resolution, would enable the analysis of combinatorial effects of such conditions on cellular phenotypes, including additive and/or nonlinear effects. Design-wise, this could be achieved by superimposing orthogonal flow-free diffusion-based gradients (*23*) and using several sets of fluorescence sensor particles.

MATERIALS AND METHODS

Microfluidic device design and fabrication

The microfluidic module is a mixer-based gradient-generating device adapted from Jeon *et al.* (*52*) with modifications. It is composed of a three-level cascade of T-junctions creating a dilution series of two input solutions at different pH and a gradient observation chamber (Fig. 2A). The mixing serpentine channels are 100 μm wide, and the length of them at each level is calculated to ensure total mixing based on the diffusion coefficient of hydronium ion H_3O^+ at 25°C of 9.3×10^{-9} m^2/s (*53*). The dimensions of the obversion chamber are 5 mm by 5 mm to match the dimensions of the Visium spatial transcriptomic slide. The channel height is 100 μm. An array of pillars with a diameter of 200 μm was added to the observation chamber to prevent collapse during assembly. The master mold was prepared using SU-8 photolithography on a silicon substrate (fig. S1). Briefly, SU-8 2075 with a thickness of 100 μm was spin-coated (Spin Coater: RCD8) on hexamethyldisilazane (HMDS)-pretreated silicon wafer, and the microchannel pattern was exposed on to the SU-8 substrate in Maskless Aligner (Maskless 01). After development, the pattern was antistiction-coated by Molecular Vapor Deposition (MVD 100 Molecular Vapor Deposition System). A PDMS replica of the mold was made. The SYLGARD 184 Silicone Elastomer Kit, with monomer and crosslinker mixed at the weight ratio of 10:1, was poured into the master mold and cured in the oven at 80°C for 2 hours. After curing, the PDMS slab was peeled off the mold and cut to the dimensions of a glass slide (76 mm by 26 mm). To avoid air bubbles in the experiment, two air traps were added in the microfluidic device. To make air traps, PDMS replica with 3-mm thickness was firstly obtained, and two holes with 3 mm were punched out in the two inlet channels, another 1-mm flat PDMS was fabricated and cut the same dimension as the 3-mm PDMS replica, and then the two pieces of PDMS were oxygen plasma–treated, aligned, and bonded together (fig. S1). Last, fluidic connections to the channels were made by punching holes through the PDMS slab using tissue biopsy punch (Harris Uni-core, 1 mm in diameter).

In an alternate method, we also prepared a mold using 3D printing. Briefly, the designed file was transferred to stereolithography (SLA) 3D printer (Form 3B), and black resin (Formlabs) was printed with a layer thickness of 25 μm. The printed master mold was immersed into an isopropanol ultrasonic bath to remove uncured resin and placed in an ultraviolet cure box for complete curing at 60°C for 30 min for complete curing. In this case, to get the PDMS replica, the mixer of SYLGARD 184 was cured in the oven at 65°C for 48 hours (*54*).

To make the workflow accessible for labs with no access to a clean room facility, we also prepared a mold for casting the PDMS chip with similar design (fig. S7A). 3D printing gives a less good control over dimensions (down to 25 μm with our SLA 3D printer). Because of the resolution limitation of our 3D printing, the printed mold's actual dimensions could affect the functionality of the microfluidic device. We thus designed a test structure with two symmetric flow channels at an identical designed cross-sectional area of 50 μm by 50 μm. After fabrication of the 3D-printed mold and casting of the PDMS device, we measured the channels' cross-sectional area at 50 different positions using scanning electron microscopy (SEM) images (fig. S7B). To do SEM imaging of the PDMS cross section, the PDMS device was cut through by a scalpel in a direction that was perpendicular to the channels' direction, and then the cut sample was mounted on a vertical SEM holder. We found a difference of 18% of the mean cross-sectional areas of the two parallel flow channels, and the fidelity of the printed mold to the design was worthy for the depth. A second concern for our microfluidic design was the ability to create support pillars. The pillars were designed as cylinders; however, they are fabricated as cones (fig. S7C). However, this is not critical as the height of the cones was sufficient to support the ceiling of the observation chamber. The variation of the channel dimensions may affect the hydraulic resistance and thus endanger the mixing ratio in the gradient-generating channels. Therefore, we mitigate this effect by driving the flow at a fixed flow rate rather than a fixed pressure. We show that we can generate a fluorescein gradients profile in the PDMS device fabricated from a 3D-printed mold (fig. S7D) that is similar to the fluorescein gradient generated in the clean room fabricated device shown in the section "Microfluidic device design" (Fig. 2E).

Mounting of the collagen I layer in the device: General procedures

A collagen I layer, with or without cells, was prepared on a microscope glass slide used as a lid for the microfluidic device (Fig. 2B). A frame of pressure adhesive tape (adhesive, optical, thickness of 150 μm, MicroAmp) was cut by CO_2 laser cutting (Epilog laser mini 3). External dimensions of 25 mm by 75 mm fit a standard microscope slide, and a window of 6 mm by 6 mm fits the position of the gradient observation channel on the PDMS device. The window area is slightly larger than that of the gradient observation channel to make sure the gradients in the collagen I layer covers the whole range of generated gradients. The frame was laminated on a positively charged glass slide (Premium Printer Slides, VWR). For 200 μl of collagen solution (6 mg/ml), we mixed 20 μl of 10× PBS, 29.2 μl of MilliQ water, 3.4 μl of 1 M NaOH, and 147.4 μl of Rat tail collagen I (8.14 mg/ml; #354249, Corning). The collagen solution was dropped into the frame on a glass slide, covered with a thin fluorinated ethylene propylene (FEP) film, loaded with a glass slide on top to keep the FEP film flat, and let to gelated at 37°C for 1 hour. After gelation, the FEP film and the top glass slide were lifted up, and the collagen I layer was kept in PBS or cell culture medium until use.

Assembling the microfluidic platform and generation of gradients

The PDMS microfluidic device and the glass slide with the collagen I layer were held together with a home-made PMMA holder comprising fluidic connectors and a metal frame (Fig. 1C). Screws to maintain the reversible sealing were adjusted at a maximum torque of 4 N·m. Pressure-based flow controllers (Fluigient, Flow EZ) were used to drive the liquid flow. Two tubes of solutions, PBS or media with different pH, were connected with the flow controllers. Two flow rate sensors (Flow Unit M, Fluigent) were also added to control the flow rate of the whole microfluidic platform. The flow rate sensors were used here to make the microfluidic platform work constantly and stably. The pressure distribution is the key factor in the mixer-based gradient-generating device to mix and divide solutions into the concentrations wanted. Many factors, such as the hydrostatic pressure in connection tubing and dimension inaccuracy during 3D printing, may affect the pressure distribution. Therefore, controlling the flow rate rather than the pressure can provide a more stable pressure distribution in the microfluidic platform.

The tubing connecting flow controllers, flow rate sensors, and the chip holder were prefilled with solutions to remove all the air. Next, the oxygen plasma–treated PDMS microfluidic device was put on the

top of the chip holder with all inlet and outlet holes aligned. The PDMS microfluidic device was then covered with PBS before the glass slide with the collagen film facing down assembled on top of PDMS. The collagen layer was aligned with the gradient observation area of the PDMS device. The initial flow rates of both inlets were set to 10 μl/min to check for air bubbles and leaking. After that, solutions were supplied at flow rates of 5 μl/min to generate stable gradients in the gradient observation channel. The gradient profile was visualized by fluorescence microscopy. First, we validated the overall functionality using a gradient of fluorescein sodium salt (#F6377, Sigma-Aldrich) from 2 to 0 mg/ml. Next, we generated a pH gradient of 6.0 to 7.4, which we visualized using 5-(and-6)-carboxy SNARF-1 (#C1270, Thermo Fisher Scientific). Ratiometric measurement was performed using excitation at 488 nm and emission filters of 582/75 and 698/70 nm. Nonratiometric measurement was done using green light-emitting diode excitation (excitation: 500 to 750 nm) and red emission (emission: 605 to 660 nm) (fig. S2). To determine the pH gradient across the observation chamber, a calibration experiment was performed in which the SNARF ratiometric signal was determined as a function of pH, using six KCl Ringer solutions (140 mM KCl, 1 mM K_2HPO_4, 1 mM $CaCl_2$, 0.5 mM $MgCl_2$, 25 mM Hepes, and pH adjusted by adding 1 M HCl or 1 M NaOH) of known pH and determining the ratio of fluorescence intensities at two emission values.

Cell lines and culture conditions

MDA-MB-231 human breast cancer cells (ATCC-HTB-26) were cultured in Dulbecco's modified Eagle's medium, high glucose, and pyruvate (#41966, Thermo Fisher Scientific), supplemented with 10% (v/v) fetal bovine serum (#F9665, Sigma-Aldrich) and 1% (v/v) penicillin-streptomycin (#P0781, Sigma-Aldrich), at 37°C in a 95% humidified incubator with 5% CO_2, and passaged when about 80% confluent. Cell identity was validated by short tandem repeat (STR) profiling, and mycoplasma-free status was confirmed every 2 to 3 months using VenorGEM Classic (#11-1025, Minerva Biolabs, Berlin, DE).

To prepare the collagen I/cell layers, cells were detached with trypsin (#T4174, Sigma-Aldrich) and gently pelleted [250 relative centrifugal force (rcf), 5 min]. The growth medium was removed, cells were resuspended in 200 μl of cold medium and counted, and the appropriate volume to obtain a final concentration of 4×10^6 cells/ml after mixing with collagen I was determined. The cell-containing collagen I solution (15 μl) was added into the device frame as described in the "Mounting of the collagen I layer in the device: General procedures" section. After 1 hour of gelation, growth medium was added on top of the collagen I/cell layers, and the slides were placed in the 37°C/5% CO_2 incubator until use on day 3 after preparation for pH gradient experiments.

For pH gradient studies, the growth medium (same as above) was used at ambient pH (7.5 CO_2 incubator) or adjusted to pH 6.0 or 6.4. To reach pH 6.4 or 6.0, 290 or 305 μl of 1 M HCl, respectively, was added to 10-ml medium. Because of the composite pH buffering in growth media (*55*), these amounts were empirically determined at 5% CO_2 using fine-grained pH strips (#109543, Merck).

For the Visium TO experiments, patterned collagen I/cell layers were generated: Two collagen I solutions were prepared as above, one with cells at the final concentration of 4×10^6 cells/ml and one without addition of cells. Eight microliters of the solution with cells was added following a horizontal line on the top part of the frame, and 8 μl of the solution without cells was added following a horizontal line on the bottom side of the frame. Subsequent steps were as above.

Analysis of cell motility

Experimental procedure

After assembling the microfluidic device on the glass slide, the pH gradient was generated, as detailed in the "Assembling the microfluidic platform and generation of gradients" section. The cells were imaged in bright field as a z-stack (5-μm step size, 25 slices) every 10 min for 4 hours, using a Nikon Ti2-E microscope with an environmental control chamber (5% CO_2, 90% humidity), 20× objective, and a Kinetix Teledyne Photometrics camera. Five regions along the pH gradient and three along the pH-independent axis were imaged in this manner (Fig. 3A).

Data analysis

Image stacks were preprocessed in Fiji, applying a mean intensity projection to enable visualization of cells from all z-slices in a single slice. The images were then processed using the deep learning–based segmentation method Cellpose (*33*) for cell detection: The "cyto" pretrained model was used, and the regions of interest obtained were manually corrected on 10 images. The obtained custom model was then used in all movies to detect and track the cells positions, using the TrackMate Fiji plugin (*34*). The positions of the cells were further analyzed using a home-made MATLAB script. First, the global x and y drift of the sample was measured using a dead cell as fiducial marker on a separate field of view. This lateral drift was then subtracted from all cell tracks in all other field of views of the experiment. Then, all the cell tracks were normalized by their first coordinates. Last, step size was plotted in micrometers.

Live/dead staining

Experimental procedure

To assess cell viability after applying a pH gradient, the microfluidic device was opened by gently opening the screws, a solution of 3 μM calcein-AM (#C3099, Thermo Fisher Scientific) and 3 μM PI (#P3566, Thermo Fisher Scientific) in PBS was added on top of the collagen I/cell layer, and the slide was incubated for 15 min at 37°C. After incubation, the solution was removed, and the collagen I/cell layer was rinsed two times with PBS. After staining and rinsing, collagen I/cell layers were imaged using epifluorescence microscopy, using excitation wavelengths of 488 (calcein) and 575 (PI) nm, 20× objective, a Kinetix Teledyne Photometrics camera, and a 4′,6-diamidino-2-phenylindole (DAPI)/green fluorescent protein (GFP)/mCherry triple band emission filter set. Z-stacks (30 to 60 optical sections) were acquired in 25 different positions: 5 positions along the pH gradient and 5 regions as technical replicates at each of these positions along the y axis, since there is no pH gradient along this axis.

Data analysis

From the z-stacks, maximum intensity projections were obtained using Fiji. The same threshold was applied for all positions, respectively, at 488 and 575 nm. The cells were then automatically detected using the "Analyze particles" plugin of Fiji, applying a size filter to only count single cells. After quantifying the cells in 488- and 575-nm fluorescence, the viability was obtained by calculating the ratio of calcein-stained (i.e., live) cells over the sum of PI- and calcein-stained cells (i.e., live + dead cells).

IF analysis

Experimental procedure

For IF analysis, the device was opened after 4 hours of application of the pH gradient, and the glass slide with the collagen I/cell layer was retrieved. The layer was rinsed with cold PBS, and cells were fixed in 4% paraformaldehyde (#9713.1000, VWR) for 15 min at room temperature, washed 2 × 5 min in tris-buffered saline with 0.1% Tween (TBST), permeabilized with 0.5% Triton X-100 (#7-1315-01, PlusOne) in TBST for 5 min, and blocked with 5% bovine serum albumin (BSA; #A7906, Sigma-Aldrich) in TBST for 30 min. Primary antibodies against Ki-67 (#9449, Cell Signaling Technology) and cleaved PARP-1 (#5625, Cell Signaling Technology) diluted in 1% BSA and TBST (1:100 in both cases) were added, and the slide was incubated overnight at 4°C in a humid chamber. Next day, cells were washed with 1% BSA in TBST (3 × 5 min), incubated with secondary antibodies (#A-11070 and #A10037, Invitrogen) in TBST + 1% BSA (1:600 dilution) for 2 hours at room temperature, lastly washed 5 min with 1% BSA in TBST, incubated 5 min with DAPI (#D3571, Invitrogen) (1:1000 dilution in TBST + 1% BSA), and washed 3 × 5 min in TBST + 1% BSA. The collagen I/cell layers were imaged using epifluorescence microscopy, with excitation wavelengths of 380 nm (DAPI), 488 nm [cleaved (c-)PARP-1], and 575 nm (Ki-67), 20× objective, a Kinetix Teledyne Photometrics camera, and a DAPI/GFP/mCherry triple band emission filter set. Z-stacks (30 to 60 slices) were acquired in 25 different positions following the same grid used during the pH gradient image acquisition (see Fig. 4B).

Data analysis

From these z-stacks, maximum intensity projections were obtained using ImageJ. The same thresholds were applied for all positions, in the 380-, 488-, and 575-nm stacks. Cells were then automatically detected using the "Analyze particles" plugin of Fiji, applying a size filter to only count single cells. After quantifying the cells at 380, 488, and 575 nm, apoptosis and proliferation fractions were obtained by calculating the number of cells at 488 nm per number of cells at 380 nm (apoptotic cells) and the number of cells at 575 nm per number of cells at 380 nm (proliferating cells).

OCT freezing of collagen I/cell layers

MDA-MB-231 cells embedded in collagen I on a glass slide were prepared as described above. The collagen I/cell layers were fixed in methanol for 20 min, and residual methanol was wiped off. For Visium TO and Visium spatial GEX experiments, a bright-field overview image was taken for each glass slide before methanol fixation, to verify that all collagen layers had a comparable cell density. For freezing, a 7 mm by 7 mm silicone isolator sheet material (0.25-mm thick) (#GBL664475-5EA, Sigma-Aldrich), cut using a CO_2 laser cutting machine, was placed on the glass slide around the collagen I layer. The window area of the silicone membrane is slightly larger than that of the gradient observation channel to allow addition of excess OCT surrounding the collagen I/cell layer for the detachment of the OCT/collagen I block from the PLL glass slide. Thirty-five microliters of OCT compound (#361603E, VWR) was added on top of the cells and then transferred to an aluminum cooler block prechilled in dry ice with another glass slide placed on top to evenly spread the OCT. The OCT/collagen I block froze within a few seconds and was subsequently stored at −80°C in a sealed container until processing for either RNA extraction, Visium TO, or Visium spatial GEX experiments, within a maximum of 4 weeks from OCT freezing. To detach the OCT/collagen I block, the setup was warmed for a few seconds on the PLL glass slide side using a scalpel, and the two glass slides were disassembled. The bottom left corner of the frozen OCT/collagen I block (corresponding to the gradient side subjected to pH 6 media) was marked with a blue pen. To detach the frozen OCT/collagen I block, the pressure adhesive tape was slowly peeled off to lift the frozen OCT/collagen I block from the PLL glass slide. The excess OCT surrounding the gradient helped to keep the block attached to the pressure adhesive tape upon detachment from the PLL glass slide. Once detached, the excess OCT surrounding the OCT/collagen I block was cut off using a cold scalpel.

Morphology and RNA quality control from cells in OCT/collagen I blocks

For morphology assessment following OCT-based treatment, collagen I/cell layers were prepared as described in the "Cell lines and culture conditions" section. OCT-based treatment of the collagen I/cell layer was carried out as described in the "OCT freezing of collagen I/cell layers" section and frozen into OCT/collagen I blocks were thawed at room temperature, and OCT was slowly rinsed off with 1 ml of PBS added on top of the collagen I layer. Last, the transferred collagen I/cell layer was stained with H&E and imaged on the NanoZoomer-XR Digital slide scanner (C12000-01, Hamamatsu) at the BRIC Histology and Microscopy Core Facility, University of Copenhagen. Methanol controls were prepared and imaged in the same manner but without OCT-based treatment.

For RNA quality control (QC) assessment following OCT-based treatment, collagen I/cell layers were prepared as described in the "Cell lines and culture conditions" section, with the exception that a larger adhesive tape was used to enable extraction of a higher amount of RNA for quality assessment. In this case, a frame of pressure adhesive tape (adhesive, optical, thickness of 150 μm, MicroAmp) was cut by CO_2 laser cutting, with external dimensions 25 mm by 75 mm to fit a standard microscope slide and three windows of 17 mm by 14.5 mm. OCT treatment of the collagen I/cell layer was carried out as described in the "OCT freezing of collagen I/cell layers" section but using a larger a silicone sheet with external dimensions of 25 mm by 75 mm and a window of 17 mm by 49 mm, cut using a razor blade, and a higher volume of OCT compound (100 μl) due to the larger area. The slide containing the frozen OCT/collagen I block was thawed at room temperature, and then the OCT was slowly rinsed off with 1 ml of PBS added on top of the collagen I layer (10×) and lastly transferred to 1.5-ml LoBind tubes (0030108051, Eppendorf) for subsequent RNA extraction. Methanol-only controls were prepared in the same manner but without freezing in OCT and were then transferred to 1.5-ml LoBind tubes (0030108051, Eppendorf) for subsequent RNA extraction. RNA was extracted with TRIzol reagent (15596026, Thermo Fisher Scientific) using the Purelink Mini RNA extraction kit (12183025, Thermo Fisher Scientific) and Phasemaker tubes (A33248, Thermo Fisher Scientific) according to the manufacturer's instructions. The RNA samples were deoxyribonuclease I–treated (EN0523, Thermo Fisher Scientific) and repurified using the Purelink RNA Mini kit. RNA quality was assessed using the RNA Nano Bioanalyzer kit (5067-1511, Agilent).

Modified Visium TO method

Seven OCT/collagen I blocks, frozen as described above, were carefully placed on the seven capture areas of the Visium TO slide while on dry ice. The slide containing the OCT-frozen collagen I layer was thawed at room temperature, and the OCT compound was carefully

rinsed off with PBS. The slide was dried for 5 min on the 10x Genomics thermocycler adapter, placed on a thermocycler set to 37°C, and fixed in methanol for 5 min. The TO slide was directly H&E-stained according to the Visium H&E Staining guide (10x Genomics, CG000160) but excluding the methanol fixation step and imaged on an EVOS M7000 system (Invitrogen) using the 10× objective and on the bright-field channel. Immediately after imaging, the slide was processed according to the Visium TO user guide (10x Genomics, CG000238), and the fluorescence signal was imaged using the EVOS M7000 system using the 10× objective and red fluorescent protein channel.

Modified Visium spatial GEX method

Three OCT-frozen collagen I/cell layers, frozen as in the "OCT freezing of collagen I/cell layers" section, were carefully placed on the three capture areas of a Visium GEX slide while on dry ice. The slide containing the OCT-frozen collagen layer was thawed at room temperature and rinsed five times with 1 ml of PBS added on top of the collagen I layer, to remove any residual OCT. The slide was dried, H&E-stained, and imaged on an EVOS M7000 system (Invitrogen) using the 10× objective and on the bright-field channel. Immediately after imaging, the slide was processed according to the Visium spatial GEX user guide (10x Genomics, CG000239 Rev. F). The collagen I/cell layer was permeabilized for 8 min at 37°C, followed by reverse transcription, second-strand synthesis, denaturation, and cDNA amplification according to the Visium spatial GEX user guide (CG000239 Rev. F). The cDNA cycle number determination was carried out by performing a quantitative polymerase chain reaction (qPCR) test on a 384-well plate using the Quantstudio 7 Flex system (Thermo Fisher Scientific). The qPCR data for each sample were analyzed using R, with the threshold to determine the Cq value set at 25% of the peak fluorescence (ΔRn) value on the amplification curve. On the basis of this, a total of 14 cycles was chosen for the cDNA library amplification for all three libraries (fig. S4A). The amplified library was quantified using the High Sensitivity DNA Bioanalyzer kit (5067-4626, Agilent), with an average library length of 1034 bp across all three libraries and total cDNA yield between 500 and 850 ng (fig. S4B). Library fragmentation, end repair, A-tailing, adapter ligation, and indexing were carried out according to the Visium spatial GEX user guide (CG000239 Rev. F). The Dual Index Plate TT set A (1000215, 10x Genomics) was used for the sample indexing, with 15 amplification cycles (index sequences used are provided in table S1). Size selection and clean-up were performed using SPRIselect reagent (B23318, Beckman Coulter). The resulting library was verified using the High Sensitivity DNA Bioanalyzer kit (5067-4626, Agilent), with an average length of 483 bp (fig. S4C). The quantity of all libraries was assessed using the Qubit double-stranded DNA High Sensitivity assay (Q32854, Thermo Fisher Scientific) on a Qubit 2 fluorometer and the KAPA library quantification kit–Illumina-uni (KK4824, Roche) with the KAPA library quantification DNA control standard (7960417001, Illumina). Each library was normalized, pooled, denatured, and diluted according to the recommendations for a NovaSeq 6000 run. The final loading concentration was 300 pM, with a 1% PhiX control spike-in (FC-110-3001, Illumina). The pooled library was sequenced on a NovaSeq 6000 (Illumina) using the S1 reagent kit v1.5, 100 cycles (20028319, Illumina) at the Flow Cytometry and Single Cell Core Facility at the University of Copenhagen. Paired-end, dual-indexed sequencing was carried out on the pooled library with the following parameters, 28 cycles for read 1, 10 cycles for the i7 index, 10 cycles for the i5 index, and 90 cycles for read 2.

Visium spatial GEX data processing

Before data processing on the Space Ranger pipeline, capture areas A1 (corresponding to replicate 1) and C1 (corresponding to replicate 3) H&E images were manually aligned using the Loupe browser (version 6.4.1, 10x Genomics) to exclude the spots within the transferred collagen I/cell layer that do not contain cells. The sequencing data were demultiplexed using the unique sample index barcodes in both i7 and i5 index reads by the Single Cell Core Facility at the University of Copenhagen (see table S1 for index sequences used for each replicate). The demultiplexed reads were then processed using the Space Ranger pipeline (version 2.0.1, 10x Genomics), and the reads were aligned to the prebuilt human reference provided by 10x Genomics (GRCh38-2020-A, GENCODE v32/Ensembl 98). All the analyses below were performed with R.4.2.2 (https://R-project.org/). Data were loaded with the Seurat package (v4.9.9) (*38*). ggplot (v2.3.4.1) (*56*) and ggprism (https://csdaw.github.io/ggprism/) packages were used to draw the figures. UMI counts for each gene in each spot were quantified with Space Ranger. We used Seurat to read the UMI count matrices and integrate them. Log-normalized UMI counts in seurat slot "data" were used for the following analysis, including linear modeling and gene expression. To assess the influence of the pH on each gene's expression, we estimated pH dependency for each gene using MIC based on MICtools (*57*). As MIC assesses both linear (i.e., expression changes monotonically with the change of pH in a relative constant rate) and nonlinear dependence relations, we used nonlinearity score (MIC–Pearson's R^2), which was proposed in (*58*) to distinguish between nonlinearly and linearly pH-dependent genes. Both Pearson's R and MIC were calculated on the basis of pooled log UMI counts across all three replicates. As nonlinear dependence can be attributed to many different patterns, we identified such patterns using hierarchical clustering ($k = 50$, complete linkage, distance method = euclidean), with median gene expression profiles along x coordinates as inputs. The median expression of genes on the x coordinates was obtained from the bin median (50 by 50 bins across x and y axes) of each Visium capture area. To assess the reproducibility of expression profiles across replicates, we calculated the average Pearson's correlations of 50 by 50 bin medians between pairs of Visium capture areas and averaged those correlations across all pairs of replicates. As for most pH-dependent genes, there is a pH gradient along the capture areas' x coordinates, and we used a linear model with the formula log-normalized counts ~ x-axis position to assess linearity for each gene. The returned t values (t_x) were then used as an indicator of the linear relationship between pH and a given gene expression: A positive t value indicates a gene whose expression increases along the x axis and vice versa. For Fig. 7, we chose to display the genes whose the t value satisfy $|t_x| > 7$ and $\text{sign}[t_x(\text{replicate 1})] = \text{sign}[t_x(\text{replicate 2})] = \text{sign}[t_x(\text{replicate 3})]$. To control gene expression variations along the y axis, we fitted a similar linear model along the y-axis coordinates (fig. S5, B, E, and F). For Fig. 7B, the capture areas were divided into 100 quantiles along the x axis, in which the gene average expressions were calculated. These expressions were z-score–normalized (centered and standardized), and the z-scores were smoothened by local polynomial regression fitting. In the average panel (Fig. 7B, rightmost column), we show the mean of the smoothened z-scores per quantile across the different replicates. Gene set enrichment analysis was performed with the clusterProfiler package (v4.7.1) (*59*), ranking the genes according to their average t value as defined above across the three replicates. Gene Ontology term and KEGG pathway (*41*) annotations were used as gene sets, and P values were

adjusted for multiple testing using the false discovery rate correction method.

Supplementary Materials

This PDF file includes:
Figs. S1 to S7
Tables S1 and S2
Legends for movies S1 to S3

Other Supplementary Material for this manuscript includes the following:
Movies S1 to S3

REFERENCES AND NOTES

1. B. Heit, S. Tavener, E. Raharjo, P. Kubes, An intracellular signaling hierarchy determines direction of migration in opposing chemotactic gradients. *J. Cell Biol.* **159**, 91–102 (2002).
2. A. E. Schloop, P. U. Bandodkar, G. T. Reeves, Formation, interpretation, and regulation of the *Drosophila* Dorsal/NF-κB gradient. *Curr. Top. Dev. Biol.* **137**, 143–191 (2020).
3. H. Kondo, C. D. H. Ratcliffe, S. Hooper, J. Ellis, J. I. MacRae, M. Hennequart, C. W. Dunsby, K. I. Anderson, E. Sahai, Single-cell resolved imaging reveals intra-tumor heterogeneity in glycolysis, transitions between metabolic states, and their regulatory mechanisms. *Cell Rep.* **34**, 108750 (2021).
4. T. Baslan, J. Hicks, Unravelling biology and shifting paradigms in cancer with single-cell sequencing. *Nat. Rev. Cancer.* **17**, 557–569 (2017).
5. E. Boedtkjer, S. F. Pedersen, The acidic tumor microenvironment as a driver of cancer. *Annu. Rev. Physiol.* **82**, 103–126 (2020).
6. C. Corbet, E. Bastien, J. P. Santiago de Jesus, E. Dierge, R. Martherus, C. Vander Linden, B. Doix, C. Degavre, C. Guilbaud, L. Petit, C. Michiels, C. Dessy, Y. Larondelle, O. Feron, TGFβ2-induced formation of lipid droplets supports acidosis-driven EMT and the metastatic spreading of cancer cells. *Nat. Commun.* **11**, 454 (2020).
7. V. Estrella, T. Chen, M. Lloyd, J. Wojtkowiak, H. H. Cornnell, A. Ibrahim-Hashim, K. Bailey, Y. Balagurunathan, J. M. Rothberg, B. F. Sloane, J. Johnson, R. A. Gatenby, R. J. Gillies, Acidity generated by the tumor microenvironment drives local invasion. *Cancer Res.* **73**, 1524–1535 (2013).
8. D. Czaplinska, R. Ialchina, H. B. Andersen, J. Yao, A. Stigliani, J. Dannesboe, M. Flinck, X. Chen, J. Mitrega, S. P. Gnosa, O. Dmytriyeva, F. Alves, J. Napp, A. Sandelin, S. F. Pedersen, Crosstalk between tumor acidosis, p53 and extracellular matrix regulates pancreatic cancer aggressiveness. *Int. J. Cancer* **152**, 1210–1225 (2023).
9. M. G. Rolver, L. K. K. Holland, M. Ponniah, N. S. Prasad, J. Yao, J. Schnipper, S. Kramer, L. Elingaard-Larsen, E. Pedraz-Cuesta, B. Liu, L. A. Pardo, K. Maeda, A. Sandelin, S. F. Pedersen, Chronic acidosis rewires cancer cell metabolism through PPARα signaling. *Int. J. Cancer* **152**, 1668–1684 (2023).
10. P. Lee, N. S. Chandel, M. C. Simon, Cellular adaptation to hypoxia through hypoxia inducible factors and beyond. *Nat. Rev. Mol. Cell Biol.* **21**, 268–283 (2020).
11. L. Ippolito, G. Comito, M. Parri, M. Iozzo, A. Duatti, F. Virgilio, N. Lorito, M. Bacci, E. Pardella, G. Sandrini, F. Bianchini, R. Damiano, L. Ferrone, G. la Marca, S. Serni, P. Spatafora, C. V. Catapano, A. Morandi, E. Giannoni, P. Chiarugi, Lactate rewires lipid metabolism and sustains a metabolic-epigenetic axis in prostate cancer. *Cancer Res.* **82**, 1267–1282 (2022).
12. I. San-Millán, G. A. Brooks, Reexamining cancer metabolism: Lactate production for carcinogenesis could be the purpose and explanation of the Warburg Effect. *Carcinogenesis* **38**, 119–133 (2017).
13. N. Rohani, L. Hao, M. S. Alexis, B. A. Joughin, K. Krismer, M. N. Moufarrej, A. R. Soltis, D. A. Lauffenburger, M. B. Yaffe, C. B. Burge, S. N. Bhatia, F. B. Gertler, Acidification of tumor at stromal boundaries drives transcriptome alterations associated with aggressive phenotypes. *Cancer Res.* **79**, 1952–1966 (2019).
14. W. R. Wilson, M. P. Hay, Targeting hypoxia in cancer therapy. *Nat. Rev. Cancer* **11**, 393–410 (2011).
15. O. Trédan, C. M. Galmarini, K. Patel, I. F. Tannock, Drug resistance and the solid tumor microenvironment. *J. Natl. Cancer Inst.* **99**, 1441–1454 (2007).
16. M. Damaghi, J. West, M. Robertson-Tessi, L. Xu, M. C. Ferrall-Fairbanks, P. A. Stewart, E. Persi, B. L. Fridley, P. M. Altrock, R. A. Gatenby, P. A. Sims, A. R. A. Anderson, R. J. Gillies, The harsh microenvironment in early breast cancer selects for a Warburg phenotype. *Proc. Natl. Acad. Sci. U.S.A.* **118**, e2011342118 (2021).
17. A. B. Hjelmeland, Q. Wu, J. M. Heddleston, G. S. Choudhary, J. MacSwords, J. D. Lathia, R. McLendon, D. Lindner, A. Sloan, J. N. Rich, Acidic stress promotes a glioma stem cell phenotype. *Cell Death Differ.* **18**, 829–840 (2011).
18. N. Li Jeon, H. Baskaran, S. K. W. Dertinger, G. M. Whitesides, L. Van de Water, M. Toner, Neutrophil chemotaxis in linear and complex gradients of interleukin-8 formed in a microfabricated device. *Nat. Biotechnol.* **20**, 826–830 (2002).
19. S.-J. Wang, W. Saadi, F. Lin, C. Minh-Canh Nguyen, N. Li Jeon, Differential effects of EGF gradient profiles on MDA-MB-231 breast cancer cell chemotaxis. *Exp. Cell Res.* **300**, 180–189 (2004).
20. Š. Selimović, W. Y. Sim, S. B. Kim, Y. H. Jang, W. G. Lee, M. Khabiry, H. Bae, S. Jambovane, J. W. Hong, A. Khademhosseini, Generating nonlinear concentration gradients in microfluidic devices for cell studies. *Anal. Chem.* **83**, 2020–2028 (2011).
21. J. M. Ayuso, M. Virumbrales-Munoz, P. H. McMinn, S. Rehman, I. Gomez, M. R. Karim, R. Trusttchel, K. B. Wisinski, D. J. Beebe, M. C. Skala, Tumor-on-a-chip: A microfluidic model to study cell response to environmental gradients. *Lab Chip* **19**, 3461–3471 (2019).
22. B. J. Kim, M. Wu, Microfluidics for mammalian cell chemotaxis. *Ann. Biomed. Eng.* **40**, 1316–1327 (2012).
23. N. Garcia-Seyda, L. Aoun, V. Tishkova, V. Seveau, M. Biarnes-Pelicot, M. Bajénoff, M.-P. Valignat, O. Theodoly, Microfluidic device to study flow-free chemotaxis of swimming cells. *Lab Chip* **20**, 1639–1647 (2020).
24. L. Moses, L. Pachter, Museum of spatial transcriptomics. *Nat. Methods* **19**, 534–546 (2022).
25. D. C. Duffy, H. L. Gillis, J. Lin, N. F. Sheppard, G. J. Kellogg, Microfabricated centrifugal microfluidic systems: Characterization and multiple enzymatic assays. *Anal. Chem.* **71**, 4669–4678 (1999).
26. A. Yahyazadeh Shourabi, N. Kashaninejad, M. S. Saidi, An integrated microfluidic concentration gradient generator for mechanical stimulation and drug delivery. *J. Sci. Adv. Mater. Devices* **6**, 280–290 (2021).
27. P. H. Imenez Silva, N. O. Camara, C. A. Wagner, Role of proton-activated G protein-coupled receptors in pathophysiology. *Am. J. Physiol. Cell Physiol.* **323**, C400–C414 (2022).
28. P. Tohidifar, M. J. Plutz, G. W. Ordal, C. V. Rao, The Mechanism of Bidirectional pH Taxis in Bacillus subtilis. *J. Bacteriol.* **202**, e00491-19 (2020).
29. C. Stock, B. Gassner, C. R. Hauck, H. Arnold, S. Mally, J. A. Eble, P. Dieterich, A. Schwab, Migration of human melanoma cells depends on extracellular pH and Na^+/H^+ exchange. *J. Physiol.* **567**, 225–238 (2005).
30. C. Martin, S. F. Pedersen, A. Schwab, C. Stock, Intracellular pH gradients in migrating cells. *Am. J. Physiol. Cell Physiol.* **300**, C490–C495 (2011).
31. R. K. Paradise, M. J. Whitfield, D. A. Lauffenburger, K. J. Van Vliet, Directional cell migration in an extracellular pH gradient: A model study with an engineered cell line and primary microvascular endothelial cells. *Exp. Cell Res.* **319**, 487–497 (2013).
32. E. Takahashi, D. Yamaguchi, Y. Yamaoka, A relatively small gradient of extracellular pH directs migration of MDA-MB-231 cells in vitro. *Int. J. Mol. Sci.* **21**, 2565 (2020).
33. C. Stringer, T. Wang, M. Michaelos, M. Pachitariu, Cellpose: A generalist algorithm for cellular segmentation. *Nat. Methods* **18**, 100–106 (2021).
34. J.-Y. Tinevez, N. Perry, J. Schindelin, G. M. Hoopes, G. D. Reynolds, E. Laplantine, S. Y. Bednarek, S. L. Shorte, K. W. Eliceiri, TrackMate: An open and extensible platform for single-particle tracking. *Methods* **115**, 80–90 (2017).
35. P. Swietach, E. Boedtkjer, S. F. Pedersen, How protons pave the way to aggressive cancers. *Nat. Rev. Cancer* **23**, 825–841 (2023).
36. M. Flinck, S. H. Kramer, S. F. Pedersen, Roles of pH in control of cell proliferation. *Acta Physiol.* **223**, e13068 (2018).
37. D. Lagadic-Gossmann, L. Huc, V. Lecureur, Alterations of intracellular pH homeostasis in apoptosis: Origins and roles. *Cell Death Differ.* **11**, 953–961 (2004).
38. Y. Hao, S. Hao, E. Andersen-Nissen, W. M. Mauck III, S. Zheng, A. Butler, M. J. Lee, A. J. Wilk, C. Darby, M. Zager, P. Hoffman, M. Stoeckius, E. Papalexi, E. P. Mimitou, J. Jain, A. Srivastava, T. Stuart, L. M. Fleming, B. Yeung, A. J. Rogers, J. M. McElrath, C. A. Blish, R. Gottardo, P. Smibert, R. Satija, Integrated analysis of multimodal single-cell data. *Cell* **184**, 3573–3587.e29 (2021).
39. Y. A. Reshef, D. N. Reshef, H. K. Finucane, P. C. Sabeti, M. Mitzenmacher, Measuring dependence powerfully and equitably. *J. Mach. Learn. Res.* **17**, 7406–7468 (2016).
40. D. Szklarczyk, R. Kirsch, M. Koutrouli, K. Nastou, F. Mehryary, R. Hachilif, A. L. Gable, T. Fang, N. T. Doncheva, S. Pyysalo, P. Bork, L. J. Jensen, C. von Mering, The STRING database in 2023: Protein-protein association networks and functional enrichment analyses for any sequenced genome of interest. *Nucleic Acids Res.* **51**, D638–D646 (2023).
41. M. Kanehisa, M. Furumichi, Y. Sato, M. Kawashima, M. Ishiguro-Watanabe, KEGG for taxonomy-based analysis of pathways and genomes. *Nucleic Acids Res.* **51**, D587–D592 (2023).
42. A. Filatova, S. Seidel, N. Böğürcü, S. Gräf, B. K. Garvalov, T. Acker, Acidosis acts through HSP90 in a PHD/VHL-independent manner to promote HIF function and stem cell maintenance in glioma. *Cancer Res.* **76**, 5845–5856 (2016).
43. K. Mekhail, L. Gunaratnam, M.-E. Bonicalzi, S. Lee, HIF activation by pH-dependent nucleolar sequestration of VHL. *Nat. Cell Biol.* **6**, 642–647 (2004).
44. J. L.-Y. Chen, D. Merl, C. W. Peterson, J. Wu, P. Y. Liu, H. Yin, D. M. Muoio, D. E. Ayer, M. West, J.-T. Chi, Lactic acidosis triggers starvation response with paradoxical induction of TXNIP through MondoA. *PLOS Genet.* **6**, e1001093 (2010).
45. B. Albert, I. C. Kos-Braun, A. K. Henras, C. Dez, M. P. Rueda, X. Zhang, O. Gadal, M. Kos, D. Shore, A ribosome assembly stress response regulates transcription to maintain proteome homeostasis. *eLife* **8**, e45002 (2019).

46. J. Yao, D. Czaplinska, R. Ialchina, J. Schnipper, B. Liu, A. Sandelin, S. F. Pedersen, Cancer cell acid adaptation gene expression response is correlated to tumor-specific tissue expression profiles and patient survival. *Cancers* **12**, 2183 (2020).
47. S. F. Pedersen, I. Novak, F. Alves, A. Schwab, L. A. Pardo, Alternating pH landscapes shape epithelial cancer initiation and progression: Focus on pancreatic cancer. *Bioessays* **39**, 1600253 (2017).
48. A. Chen, S. Liao, M. Cheng, K. Ma, L. Wu, Y. Lai, X. Qiu, J. Yang, J. Xu, S. Hao, X. Wang, H. Lu, X. Chen, X. Liu, X. Huang, Z. Li, Y. Hong, Y. Jiang, J. Peng, S. Liu, M. Shen, C. Liu, Q. Li, Y. Yuan, X. Wei, H. Zheng, W. Feng, Z. Wang, Y. Liu, Z. Wang, Y. Yang, H. Xiang, L. Han, B. Qin, P. Guo, G. Lai, P. Muñoz-Cánoves, P. H. Maxwell, J. P. Thiery, Q.-F. Wu, F. Zhao, B. Chen, M. Li, X. Dai, S. Wang, H. Kuang, J. Hui, L. Wang, J.-F. Fei, O. Wang, X. Wei, H. Lu, B. Wang, S. Liu, Y. Gu, M. Ni, W. Zhang, F. Mu, Y. Yin, H. Yang, M. Lisby, R. J. Cornall, J. Mulder, M. Uhlén, M. A. Esteban, Y. Li, L. Liu, X. Xu, J. Wang, Spatiotemporal transcriptomic atlas of mouse organogenesis using DNA nanoball-patterned arrays. *Cell* **185**, 1777–1792.e21 (2022).
49. S. Kersten, R. Stienstra, The role and regulation of the peroxisome proliferator activated receptor alpha in human liver. *Biochimie* **136**, 75–84 (2017).
50. K. Vandereyken, A. Sifrim, B. Thienpont, T. Voet, Methods and applications for single-cell and spatial multi-omics. *Nat. Rev. Genet.* **24**, 494–515 (2023).
51. J. M. Bond, B. Herman, J. J. Lemasters, Protection by acidotic pH against anoxia/reoxygenation injury to rat neonatal cardiac myocytes. *Biochem. Biophys. Res. Commun.* **179**, 798–803 (1991).
52. N. L. Jeon, S. K. W. Dertinger, D. T. Chiu, I. S. Choi, A. D. Stroock, G. M. Whitesides, Generation of solution and surface gradients using microfluidic systems. *Langmuir* **16**, 8311–8316 (2000).
53. L. G. Longsworth, Temperature dependence of diffusion in aqueous solutions. *J. Phys. Chem.* **58**, 770–773 (1954).
54. K.-I. Kamei, Y. Mashimo, Y. Koyama, C. Fockenberg, M. Nakashima, M. Nakajima, J. Li, Y. Chen, 3D printing of soft lithography mold for rapid production of polydimethylsiloxane-based microfluidic devices for cell stimulation with concentration gradients. *Biomed. Microdevices* **17**, 36 (2015).
55. J. Michl, K. C. Park, P. Swietach, Evidence-based guidelines for controlling pH in mammalian live-cell culture systems. *Commun. Biol.* **2**, 144 (2019).
56. H. Wickham, *ggplot2: Elegant Graphics for Data Analysis* (Springer, 2009).
57. D. Albanese, S. Riccadonna, C. Donati, P. Franceschi, A practical tool for maximal information coefficient analysis. *Gigascience* **7**, 1–8 (2018).
58. Y. A. Reshef, D. N. Reshef, H. K. Finucane, P. C. Sabeti, M. Mitzenmacher, Measuring dependence powerfully and equitably. *J. Mach. Learn. Res.* **17**, 1–63 (2016).
59. G. Yu, L.-G. Wang, Y. Han, Q.-Y. He, clusterProfiler: An R package for comparing biological themes among gene clusters. *OMICS* **16**, 284–287 (2012).

Acknowledgments: We gratefully acknowledge the excellent technical assistance of M. Flinck and T. Larsen, of Cameron Hunt for the Cellpose deep learning–based segmentation of cells, and early contributions by A. Fuentes and J. Seshadri. We thank Y. Antoku from the BRIC microscopy Core Facility for expert technical assistance in microscopy imaging of Visium slides on the EVOS M7000 system, R. Klitgaard from the Flow Cytometry and Single Cell Core Facility at the University of Copenhagen for assistance with Visium library sequencing on the NovaSeq 6000, and I. Korshunova at the BRIC Single Cell Genomics Facility for help with initial Visium TO tests. Sequencing support for pilot shallow sequencing tests was provided by the BRIC Sequencing Core Facility, and H&E imaging for morphology QC was carried out with the support of BRIC Histology and Microscopy Facility. **Funding:** This work was supported by funding from the Novo Nordisk Foundation (NNF19OC0057739 to S.F.P., R.M., and A.Sa.; NNF21OC0069598 to S.F.P., R.M., A.Sa., and U.R.-G.; NNF19OC0058262 to A.Sa. and S.F.P.; and NNF20OC0059951 to A.Sa.), the Carlsberg Foundation (CF20-0491 to S.F.P. and CF19-0505 to A.Sa.), and The Danish Cancer Foundation (R325-A18868 to A.Sa. and S.F.P.). **Author contributions:** The three shared first authors contributed equally and are listed in alphabetical order. R.M., A.Sa., and S.F.P. conceived the idea. R.C., J.A., and Y.L. designed experiments, supervised by A.Sa., R.M., and S.F.P. R.C., J.A., Y.L., R.M., A.St., and Y.D. analyzed the data. R.C., J.A., Y.L., A.St., and Y.D. prepared the figures, with inputs from A.Sa., R.M., and S.F.P. U.R.-G. and I.T. performed key supporting experiments. A.Sa., R.M., S.F.P., R.C., J.A., and Y.L. collectively planned and wrote the manuscript. All authors contributed to editing of the text, and all authors read and approved the final manuscript. **Competing interests:** S.F.P. is cofounder of SOLID Therapeutics. All other authors declare that they have no competing interests. **Data and materials availability:** Visum expression data have been deposited in the GEO database with accession number GSE242233. All other data needed to evaluate the conclusions in the paper are present in the paper and/or the Supplementary Materials.

Submitted 5 December 2023
Accepted 2 April 2024
Published 3 May 2024
10.1126/sciadv.adn3448